Available online at www.sciencedirect.com

ScienceDirect

Geochimica et Cosmochimica Acta 319 (2022) 30–55

Geochimica et Cosmochimica Acta

www.elsevier.com/locate/gca

Refractory inclusions as Type IA chondrule precursors: Constraints from melting experiments

Scott A. Whattam [a,*], Roger H. Hewins [b,c], Jieun Seo [d], Bertrand Devouard [e]

[a] Department of Geosciences, King Fahd University of Petroleum and Minerals, Dhahran 31261, Saudi Arabia
[b] IMPMC, Sorbonne Univ., MNHN, UPMC Paris 06, UMR CNRS 7590, 75005 Paris, France
[c] Department of Earth and Planetary Sciences, Rutgers University, Piscataway, NJ 08854, United States
[d] Department of Earth and Environmental Sciences, Korea University, Seoul 02841, Republic of Korea
[e] Aix-Marseille Université, CNRS, IRD, CEREGE UM34, BP 80 Aix en Provence 13545, France

Received 17 August 2021; accepted in revised form 20 December 2021; Available online 29 December 2021

Abstract

The formation of chondrules involved major processes in the protoplanetary disk and therefore needs to be understood. Identifying possible precursors and the conditions of their transformation into chondrules is an essential step. Here we investigate whether refractory inclusions (RI) can be converted into Type IA chondrule analogs by isothermal heating and dynamic crystallization experiments, and report a new constraint on chondrule peak temperatures. We prepared synthetic calcium-aluminum-rich inclusions (CAI) by sintering <20 μm An + Di + Sp powder at 1200 °C and synthetic AOA analogs from crushed <5 μm Fo gel or San Carlos olivine mixed with nuggets of synthetic CAI. We used the AOA analogs as starting materials in experiments and were able to reproduce the textures and mesostasis compositions of Type IA chondrules. However, in the charges, the olivine lacks asymmetric zonation and our mesostasis compositions show olivine fractionation trends, two differences from Type I chondrules indicating the requirement of condensation of Mg and SiO in the latter. Relict spinel is present in isothermal runs up to 1550 °C, but is totally resorbed by 1600 °C. We conclude that CAI and AOA were sintered essentially at their condensation temperatures and are appropriate precursors for chondrules. Chondrules with relict spinel must have formed at <1600 °C, much lower than their liquidus temperatures (~1750 °C). Such peak temperatures are consistent with models of condensation during chondrule formation. In typical chondrules with no inclusions of AOA or CAI, spinel is an indicator of their near complete assimilation. Grains of spinel (*sensu stricto*) in chondrules are relicts of RI and constitute a largely untapped cosmochemical resource for the investigation of chondrule provenance.

Keywords: Type IA chondrules; Aluminum-rich chondrules; Refractory inclusions; Calcium-aluminum-rich inclusions (CAI); Amoeboid olivine aggregates (AOA); Solar nebula; Experimental petrology

1. INTRODUCTION

Meteorites have given us an understanding of the evolution of our solar system. Chondritic meteorites contain refractory inclusions (RI) and chondrules, among the oldest materials known (Amelin et al., 2002; Connelly and Bizzarro, 2018). These materials witnessed the earliest astrophysical, and perhaps geological, processes in the Sun's protoplanetary disk (e.g., Krot and Nagashima, 2017). Chondrules are comprised primarily of olivine, pyroxenes, Fe, Ni-metal, troilite and glass and RI include Ca-Al-rich inclusions (CAI) containing Ca-Al-rich oxides and/or silicates, and amoeboid olivine aggregates (AOA). Fine-grained and fluffy CAI (Kornacki and Wood, 1984; MacPherson and Grossman, 1984) are widely considered

* Corresponding author.
E-mail address: scott.whattam@kfupm.edu.sa (S.A. Whattam).

https://doi.org/10.1016/j.gca.2021.12.022
0016-7037/

to have formed as solids condensed from a solar or chondritic gas and many compact CAI have undergone melting. AOA contain forsteritic olivine and a Ca-Al-rich component composed of Al-diopside, anorthite and Mg-spinel. They are inferred to be annealed aggregates of high-temperature nebular condensates (Komatsu et al., 2001; Krot et al., 2004b).

The relationship between RI and chondrules, the product of widespread early melting, is crucial to understanding the early history of the solar system. RI appear to be more primitive than chondrules as they have more refractory compositions (Grossman, 1972; Wood and Hashimoto, 1993; Ebel, 2006), and their range of radiometric ages is more restricted (Connelly et al., 2012; Bollard et al., 2015) than those of chondrules. Refractory inclusions, particularly the Mg-rich AOA, are in many cases enclosed within Mg-rich chondrules (Misawa and Nakamura, 1996; Scott and Krot, 2003; Krot et al., 2005; Krot et al., 2017; Marrocchi et al., 2019a) and Al-rich chondrules (ARC, Krot et al., 2002; Zhang et al., 2020). However, chondrule fragments caught up inside RI are very rare (Itoh and Yurimoto, 2003; Krot et al., 2005).

These observations have led to suggestions that nebular condensates of AOA and CAI are major precursors of Type I (Mg-rich) chondrules (e.g., Russell et al., 2000; Krot and Keil, 2002; Krot et al., 2006a,b), suggestions amply supported by later work (e.g., Schrader et al., 2018; Marrocchi et al., 2019a). If so, the isotopic compositions of any AOA inclusions in chondrules must yield information on the timing and spatial extent of chondrule-gas interactions (e.g., Tenner et al., 2018; Williams et al., 2020). We have therefore prepared synthetic CAI and AOA materials and subjected them to isothermal heating and dynamic crystallization experiments to test their suitability to generate chondrules. Our results confirm that CAI and AOA are viable chondrule precursors and indicate the conditions under which traces of RI may have survived in chondrules.

2. ANALYTICAL AND EXPERIMENTAL METHODS

Our experiments to investigate the response of AOA to melting consist of two distinct stages. We first simulated fine-grained CAI, and made mixtures of the synthetic CAI with olivine either as (a) annealed Fo gel or as (b) crushed San Carlos olivine (SCO). Some of mixture (a) was sintered into synthetic AOA. The compositions of these three starting materials are provided in Table 1. The second stage involves isothermal and dynamic crystallization experiments on these starting mixtures, to determine whether any produced viable chondrule analogs. Details of each stage are provided below.

2.1. Starting materials

We prepared synthetic CAI material comprised of equal fractions of <20 μm An + Di + Sp (Miyakejima anorthite, Fianarantsoa diopside and Burmese aluminous spinel) and synthetic AOA, via mixtures of sintered synthetic CAI plus either SCO or Fo gel (Table 1). The CAI mixture was pressed into circa 200–300 mg cylindrical cores and suspended in Re baskets fastened to platinum sample holders and subjected to 100 h duration heating at 1200 °C. Trial and error accompanied by imaging determined that these conditions produced coherent sintered CAI starting materials. Fo sol gel was crystallized by heating at 1300 °C for 40 h (Fa_0 typically finer than ~5 μm).

The sintered CAI starting material was subsequently crushed and sieved to <43 μm before being added to either the Fo (<43 μm) or SCO (<43 μm). We sintered 35–40 mg pellets of crushed Fo mixed with 200–300 μm nuggets of the 1200 °C-100 h synthetic CAI-cores (35:65 CAI:Fo) to act as an AOA starting material. Additional mixtures of 80% annealed Fo gel or <20 μm San Carlos olivine with 20% CAI were also prepared and used as pressed pellets in experiments. In Fig. 1, the AOA-analog compositions are compared to natural CAI, AOA and chondrule compositions. They lie on an approximate mixing line from our CAI compositions and the Fo endmember, and plot in the area in which AOA and Type IA chondrules overlap.

Aside from differences in the ratios of olivine to CAI in the synthetic CAI + SCO (20:80) and the AOA (35:65, CAI:Fo) experiments, two principle differences exist. (1) In the case of the former, the olivine is San Carlos (Fo_{88}) olivine and so has an iron component which the Fo_{100} (gel) does not; and (2) in the case of former, the CAI was pre-sintered for 100 h at 1200 °C whereas in the latter, the CAI component was sintered with Fo for 200 h at 1250 °C to produce synthetic AOA staring material. These differences need be kept in mind when considering results.

2.2. Isothermal and dynamic crystallization runs

All three AOA-like compositions were used in melting and crystallization experiments. For our synthetic AOA isothermal melting experiments, the sintered AOA starting material was simply heated at the same durations and temperatures as in the runs to synthesize CAI. For the CAI + SCO (20:80 mixture) pressed pellets, isothermal heating runs were carried out at 50 °C intervals between 1250 °C and 1600 °C for 1 h.

Dynamic crystallization runs were also conducted using the synthetic CAI + SCO mixture, synthetic CAI + Fo gel (mixed as 20:80, CAI: Fo gel), and the synthetic AOA after heating at 1600 °C for 1 h and cooling at 10 °C/h and 100 °C/h. All charges of the isothermal and cooling runs were supported on Re wires and water-quenched after cooling to 1000 °C within 5 s of removal from the furnace. An oxygen fugacity of IW-0.5 was maintained in the furnace with a mixture of $CO–CO_2$ (Nazfiger et al., 1971) using high precision flowmeters. Fugacity is easily controlled within ±0.1 log units. An S-type thermocouple (Pt100-Pt90: Rh10) was calibrated against the melting point of Au (1064 °C) and Pd (1554 °C) to monitor temperature. Samples were run in a 1 atm, DelTech DT-31-VT-OS vertical furnace housed in the Department of Earth and Planetary Sciences at Rutgers University. Charges were subsequently mounted in epoxy, ground to a flat surface, polished and carbon-coated for scanning electron microscope (SEM) analysis. They were sectioned horizontally through the olivine aggregate to examine melt infiltration. High-resolution

Table 1
Normalized compositions of starting materials.

	San Carlos olivine[a]	Fo gel	Miyakejima anorthite[b]	Fianarantsoa diopside	Burmese spinel	Bulk synthetic CAI (33.3% An +33.3% Di + 33.3% Spl)	Bulk synthetic AOA (nominal) (65% Fo gel + 35% synthetic CAI)	Bulk synthetic CAI + SCO (20% synthetic CAI + 80% SCO)	Bulk synthetic CAI + Fo gel (20% synthetic CAI + 80% Fo gel)	Type Ia Chondrule average[c]	ARC average[d]	AOA average[e] (reheated, EMP)	Type C CAI average[f]
SiO_2	39.83	42.26	44.44	55.49		32.90	38.98	38.44	40.39	47.01	45.23	40.27	36.18
TiO_2	0.02		nd							0.19	0.61	0.37	1.26
Al_2O_3	0.02		35.60		71.67	36.10	12.64	7.24	7.22	4.09	14.50	8.15	32.48
FeO	11.35		0.48					9.08		1.24	3.47	5.8	0.40
Cr_2O_3	0.00									0.46	0.21	0.3	0.07
MnO	0.15									0.13	0.06	0.1	
MgO	48.49	57.74	0.21	18.62	28.33	15.65	43.01	41.92	49.32	42.67	25.44	39.41	6.84
CaO	0.13		18.80	25.89		15.35	5.37	3.17	3.07	3.67	8.62	5.47	22.52
Na_2O	0.02		0.47							0.55	1.67	0.11	0.22
K_2O											0.19	0.02	0.01
	$Fo_{88.4}$	Fo_{100}	An_{94}							$Fo_{98.9}$			
Calculated liquidus[g]	1847 °C					1355 °C	1813 °C	1790 °C	1883 °C	1743 °	1549 °	1751 °	1080 °C

Liquidus temperatures were calculated with Petrolog3 (Danushevsky and Plechov, 2011) with an oxygen fugacity of IW −0.5 (Borisov and Shapkin, 1990).

[a] Whattam et al. (2008).
[b] Milke and Metz (2002).
[c] Jones and Scott (1989).
[d] MacPherson and Huss (2005).
[e] Komatsu et al. (2001).
[f] Beckett (1986) and Wark (1987).
[g] After Herzberg (1979).

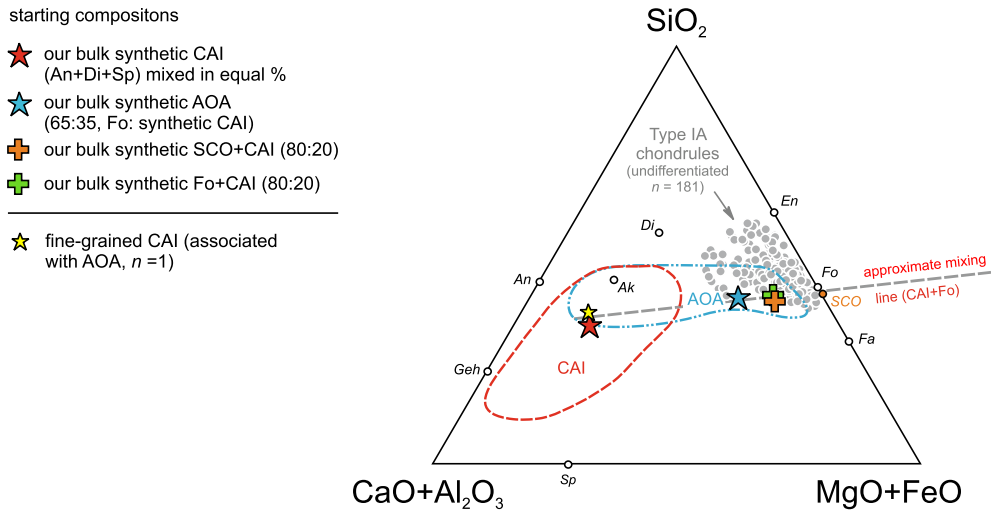

Fig. 1. Comparison of bulk compositions of natural CAI, AOA and Type IA chondrules with our synthetic CAI, CAI + Fo, CAI + SCO and AOA mixtures in CaO + Al2O3-SiO2-MgO + FeO space. Fields of Type IA chondrules, AOA and CAI are from McSween (1977a, b) and Mason and Martin (1977). Abbreviations: SCO, San Carlos olivine.

back-scattered electron (BSE) images of the charges were captured with a JEOL 6400 SEM in the Department of Earth Sciences at Carleton University, Ottawa, Canada. Images were typically taken at magnifications of 50×, 100×, 200×, 400× and 800× and enhanced with Corel Photo Shop software.

Analyses of olivine, spinel, plagioclase, and groundmass of the CAI plus San Carlos olivine charges and of AOA (CAI with Fo gel) charges were made using an electron probe micro-analyzer (EPMA, JEOL JXA–8600 SX) with energy dispersive spectroscopy (INCA–6025, Oxford Instruments) at Korea University in Seoul, South Korea. As the synthetic CAI + Fo gel runs exhibit textural and mineralogical characteristics which overlap both the AOA runs and the CAI + SCO runs (Supplementary Fig. S1), we did not probe these runs and do not discuss these runs later in great detail.

The microprobe was operated with an accelerating voltage of 15.0 kV, a beam current of 3.0 nA, a live time of 100 s, and a probe diameter of 3 μm, using ZAF correction. The following natural mineral synthetic oxides were used for calibration: quartz (Si), periclase (Mg), corundum (Al), rutile (Ti), eskolaite (Cr), manganesite (Mn), hematite (Fe), wollastonite (Ca), K-feldspar (K), and jadeite (Na). The number of analyses (n) calculated in the mean are typically ~7–10.

Details of charges (starting and final run materials) of all isothermal and dynamic crystallization runs are provided in Table 2. All EPMA probe data are provided in Supplementary Tables S1-S2 and average detection limits and standard deviations for all elements analyzed are provided in Supplementary Table S3.

3. RESULTS

3.1. Starting material sintering experiments

For the CAI composition, low temperature and low duration runs (e.g., 900 °C–50 h, see Table 2) the pressed starting powder produced a non-sintered aggregate which subsequently disaggregated when water-quenched upon removal from the furnace and formed a clastic texture of discrete unmelted grains. When heated for 100 h at 1200 °C it produced sintered CAI-like material consisting of ~10–-20 μm, subhedral spinel grains set in a fine-grained groundmass of An + Di (Fig. 2a). Its texture resembles that of a fine-grained CAI from the Nangqiang carbonaceous chondrite (Lin et al., 2005), which is shown for comparison in Fig. 2b.

Run times and/or temperatures below 100 h and 1250 °C runs on synthetic AOA powder produced materials with distinct mineral fragments and lack of textural cohesion (minor melting) (Supplementary Fig. S2, compare with Fig. 2). The 1250 °C–200 h sintered AOA-like material displays irregular, forsterite grains commonly enclosing spinel (Fig. 2c). Anorthite comprises part of the matrix but identification of discrete grains was not made. AOA from the ungrouped carbonaceous chondrite Acfer 094 (Krot et al., 2004b) is shown for comparison in Fig. 2d and our synthetic AOA closely mimics the natural one on a textural basis.

3.2. Isothermal and dynamic crystallization experiments

3.2.1. Isothermal runs

The CAI + SCO powder, used as an AOA analog, produced charges with large CAI and olivine domains demarcated by sharp contacts (Fig. 3a, b) when heated at low temperature (1250–1300 °C). Tiny pockets within the massive olivine (less than 10 um) contain Ca-Al-rich glass. By 1400 °C both the olivine and CAI domains are partly melted and begin to come apart, and discrete small (circa 20 μm) subhedral olivine crystals are apparent. By 1450 °C, some olivine grains have coarsened up to ~40 μm and are euhedral. Spinel is present up to 1550 °C. Grains continue to coarsen with temperature, reaching a maximum of ~50 μm at 1550 °C and 1600 °C, and the texture at these temperatures is similar to that of

Table 2
Experimental T, t conditions of sintering, isothermal and dynamic crystallization runs and identification of employed charges.

Synthetic CAI starting materials of An+Di+Sp mixed in equal fractions

T(°C)	Soak time (h)	Materials	Grain size (< μm)	Puck number	Charge number
900	50	An+Di+Sp	20	250	237
1150	50	An+Di+Sp	20	NA	224
1200	**100**	**An+Di+Sp**	**20**	**273**	**260**

AOA starting materials of synthetic Fo+CAI (see above) mixed as 65:35

T(°C)	Soak time (h)	Materials	Grain size (< μm)	Puck number	Charge number
1200	10	Fo+(An+Di+Sp)	5/20	271	262
1200	50	Fo+(An+Di+Sp)	5/20	271	264
1200	100	Fo+(An+Di+Sp)	5/20	271	263
1200	200	Fo+(An+Di+Sp)	5/20	271	261
1250	10	Fo+(An+Di+Sp)	5/20	272	269
1250	50	Fo+(An+Di+Sp)	5/20	272	267
1250	100	Fo+(An+Di+Sp)	5/20	272	265
1250	**200**	**Fo+(An+Di+Sp)**	**5/20**	**272**	**268**

Synthetic Fo+CAI (see above) runs mixed as 80:20

T(°C)	Soak time (h)	Olivine Added	*Grain size (< μm)	Puck number	Charge number
1250	1	Fo	5/43	417	407
1300	1	Fo	5/43	459	438
1350	1	Fo	5/43	459	439
1400	1	Fo	5/43	459	440
1450	1	Fo	5/43	459	441
1500	1	Fo	5/43	459	442
1550	1	Fo	5/43	459	434
1600	1	Fo	5/43	467	435

Synthetic SCO+CAI runs mixed as 80:20

T(°C)	Soak time (h)	Olivine added	*Grain size (< μm)	Puck number	Charge number
1250	1	SCO	20/43	417	408
1300	1	SCO	20/43	417	409
1350	1	SCO	20/43	418	411
1400	1	SCO	20/43	418	412
1450	1	SCO	20/43	418	413
1500	1	SCO	20/43	418	414
1550	1	SCO	20/43	419	415
1600	1	SCO	20/43	419	416

Synthetic AOA isothermal runs of AOA starting materials (see above)

T(°C)	Soak time (h)	Olivine added	*Grain size (< μm)	Puck number	Charge number
1300	1	Fo	43/5	450	422
1350	1	Fo	43/5	450	423
1400	1	Fo	43/5	450	425
1450	1	Fo	43/5	450	426
1550	1	Fo	43/5	451	429
1600	1	Fo	43/5	451	431

Synthetic Fo+CAI dynamic crystallization runs mixed as 80:20

T(°C)	Soak time (h)	Olivine added	Grain size (< μm)	Cooling rate (°C/h)	Puck number	Charge number
1600	1	Fo	5	100	458	446
1600	1	Fo	5	10	458	437

Synthetic SCO+CAI dynamic crystallization runs mixed as 80:20

T(°C)	Soak time (h)	Olivine added	Grain size (<μm)	Cooling rate (°C/h)	Puck number	Charge number
1600	1	SCO	20	100	458	445
1600	1	SCO	20	10	458	436

Synthetic AOA dynamic crystallization runs mixed as 65:35

(*continued on next page*)

Table 2 (*continued*)

T(°C)	Soak time (h)	Olivine added	Grain size (<μm)	Cooling rate (°C/h)	Puck number	Charge number
1600	1	Fo	5	100	457	443
1600	1	Fo	5	10	457	432

Abbreviations: Fo = Forsterite (Fa_0); SCO = (crushed) San Carlos olivine.
*Grain size of hydrocrystallized Fo 'gel' as estimated via SEM imaging.
Note that that the <20 μm 1200 °C-100 h sintered An + Di + Sp nuggets were further sieved to <43 μm before being mixed with Fo or SCO in the ratio of 80:20 (Fo: An + Di + Sp) in the isothermal and dynamic crystallization runs.
Note that Fo refers to our hydrocrystallized Fo gel (Fo_{100}).
Text in bold refers to our final synthetic CAI and AOA starting materials.
Note that trial and error accompanied with imaging determined the peak temperature and duration 1200 °C, 100 h) of the synthetic CAI and AOA (1250 °C, 200 h) starting materials (see text for further further details).
NA- (puck) not available.

classical porphyritic olivine (PO) chondrules with six-sided, euhedral olivine 'phenocrysts', skeletal olivine, and rare spinel (spinel is present in the 1550 °C run but absent in the 1600 °C run).

The synthetic AOA fragments (sintered CAI and Fo) were heated isothermally at temperatures of 1300–1600 °C, and SEM images of charges are given in Fig. 4. In the lowest temperature run (1300 °C), the charge is dominated by large (~250–800 μm diameter) forsterite masses which subsequently begin to separate by 1350 °C. In contrast to the CAI + SCO pressed powder runs, discrete olivine grains are tiny at 1350 °C (typically 10 μm) and continually coarsen, reaching about 30 μm at 1400 °C and a maximum of 60 μm at 1450 °C and 1550 °C. By

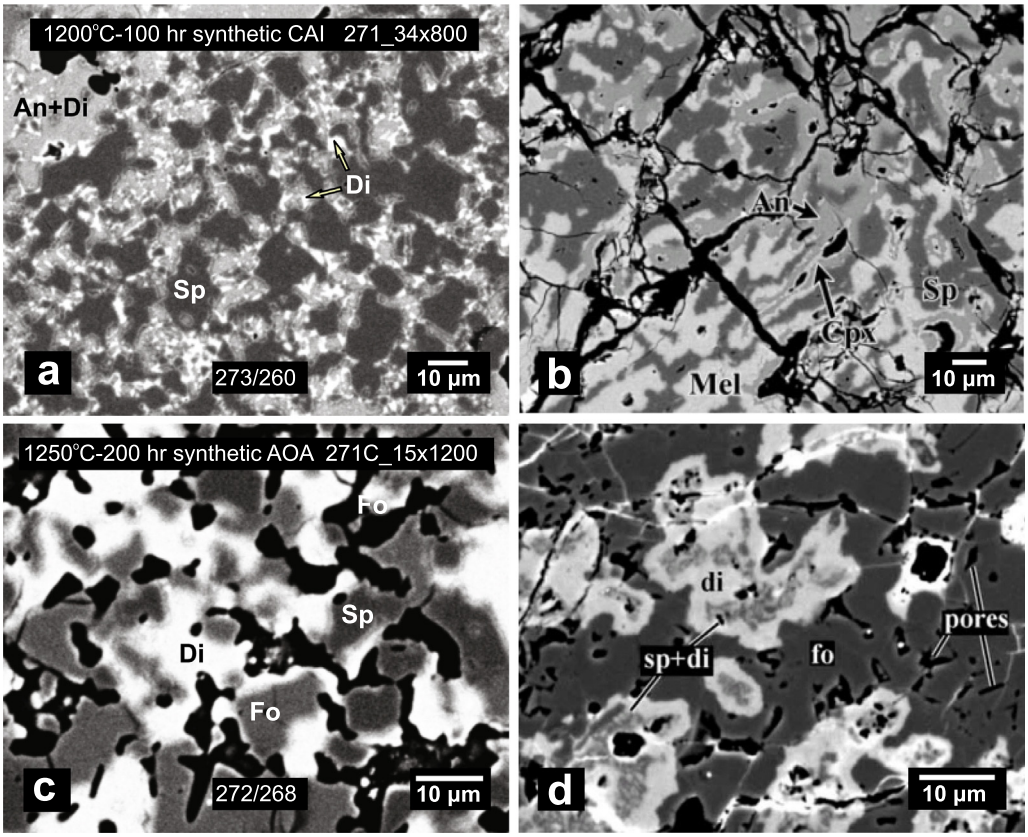

Fig. 2. Comparison of SEM images of our synthetic, sintered (a) CAI- (spinel-rich region) generated at IW −0.5 at 1200 °C for 100 hr and (c) AOA-like charges sintered at 1250 °C for 200 hr with a natural (b) CAI from the Ningqiang carbonaceous chondrite (Lin et al., 2005) and an (d) AOA from Acfer 094 (Krot et al., 2004a).

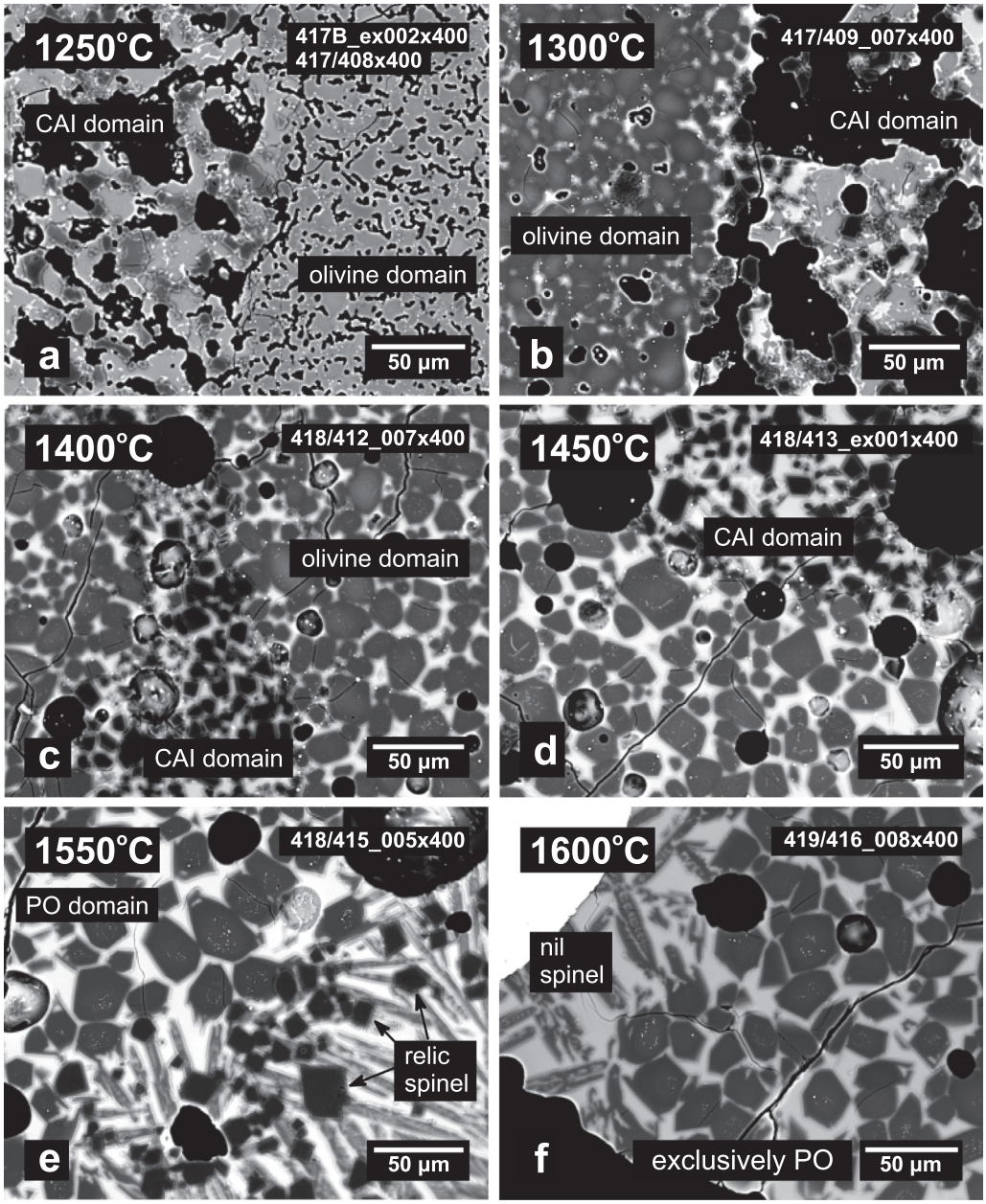

Fig. 3. SEM BSE images showing textural evolution of 1 h synthetic CAI + SCO runs (representing AOA or separate condensates) as a function of temperature.

1450 °C, a pseudo-PO texture develops but with subhedral olivine; by 1550 °C, the olivine is commonly euhedral. At 1600 °C, the texture is distinctly different from the CAI + SCO powder runs at 1600 °C which are PO. As a consequence of the higher Al content, the 1600 °C AOA run is mesostasis-rich with quench olivine and tiny (~10 µm diameter) discrete olivine phenocrysts. On the basis of EPMA data, spinel is present in all runs except for the 1600 °C isothermal run of CAI + SCO. However, spinel is not always obvious in SEM images, particularly in the higher temperatures run which contain less spinel than the lower temperature runs.

The CAI + Fo runs show a similar textural evolution to the CAI + SCO and the sintered AOA isothermal runs (Figs. 3, 4) but the Fo added as gel leads to ultimate textures which are finer grained (Supplementary Fig. S1).

3.2.2. Dynamic crystallization runs

SEM images of our synthetic CAI + SCO, CAI + Fo and our synthetic AOA dynamic crystallization runs heated at 1600 °C for 1 h before being cooled at 100 °C/h and 10 °C /h are given in Fig. 5. As in isothermal runs at high temperatures (1450–1600 °C heating for 1 hour), PO texture develops in each instance but with differences. In the syn-

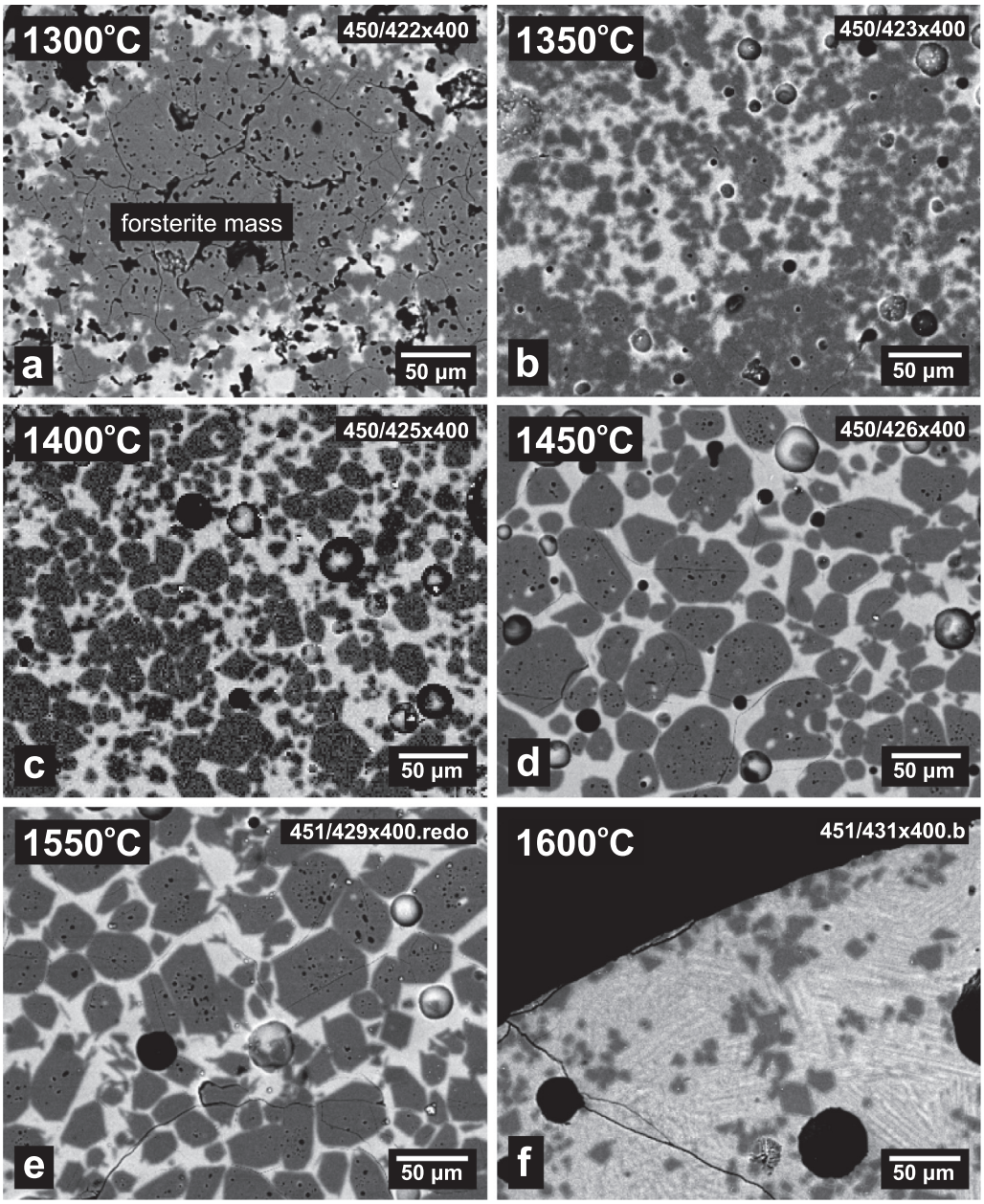

Fig. 4. SEM BSE images showing textural evolution of 1 h synthetic AOA isothermal runs as a function of temperature.

thetic CAI + SCO and synthetic CAI + Fo gel runs, there are increases in olivine grain size with decreasing cooling rate (compare Fig. 5a, c with Fig. 5b, d) as expected, and there is a textural development of (~100 µm) spinel enclosing olivine. However, and for reasons that are unclear, in the more quickly cooled AOA run (100 °C /h), texture is significantly coarser (euhedral olivine up to 100 µm) than in the slower cooled run (10 °C, with olivine up to 50 µm) and also exhibits more obvious euhedral olivine development (compare Fig. 5e with 5f).

3.3. Compositional variations in run products

Changes in phase compositions for the CAI + SCO and AOA isothermal and dynamic crystallization runs with increasing temperature and different cooling rates are shown in Figs. 6, 7 and 8. As the CAI + Fo runs have similar bulk compositions and textures to the CAI + SCO and AOA runs (compare Figs. 3, 4 with Supplementary Fig. S1 and images in Fig. 5), we do not discuss them further. Mean mesostasis compositions of our 1 h isothermal and dynamic crystallization runs are projected from $MgAl_2O_4$ (spinel) onto the plane Ca_2SiO_4 (larnite) –Mg_2SiO_4 (forsterite) – Al_2O_3 (corundum) in Fig. 6. The mesostasis and bulk composition of natural Type IA ferromagnesian chondrules (FMC), Al-rich chondrules (ARC), Type A CAI (A field), Type B CAI (B field) and Type C CAI (field C) are shown for comparison. Tables 3 and 4 provide the final phase compositions of all runs at all temperatures for the CAI + SCO and AOA charges, respectively. In Fig. 7 we show changes

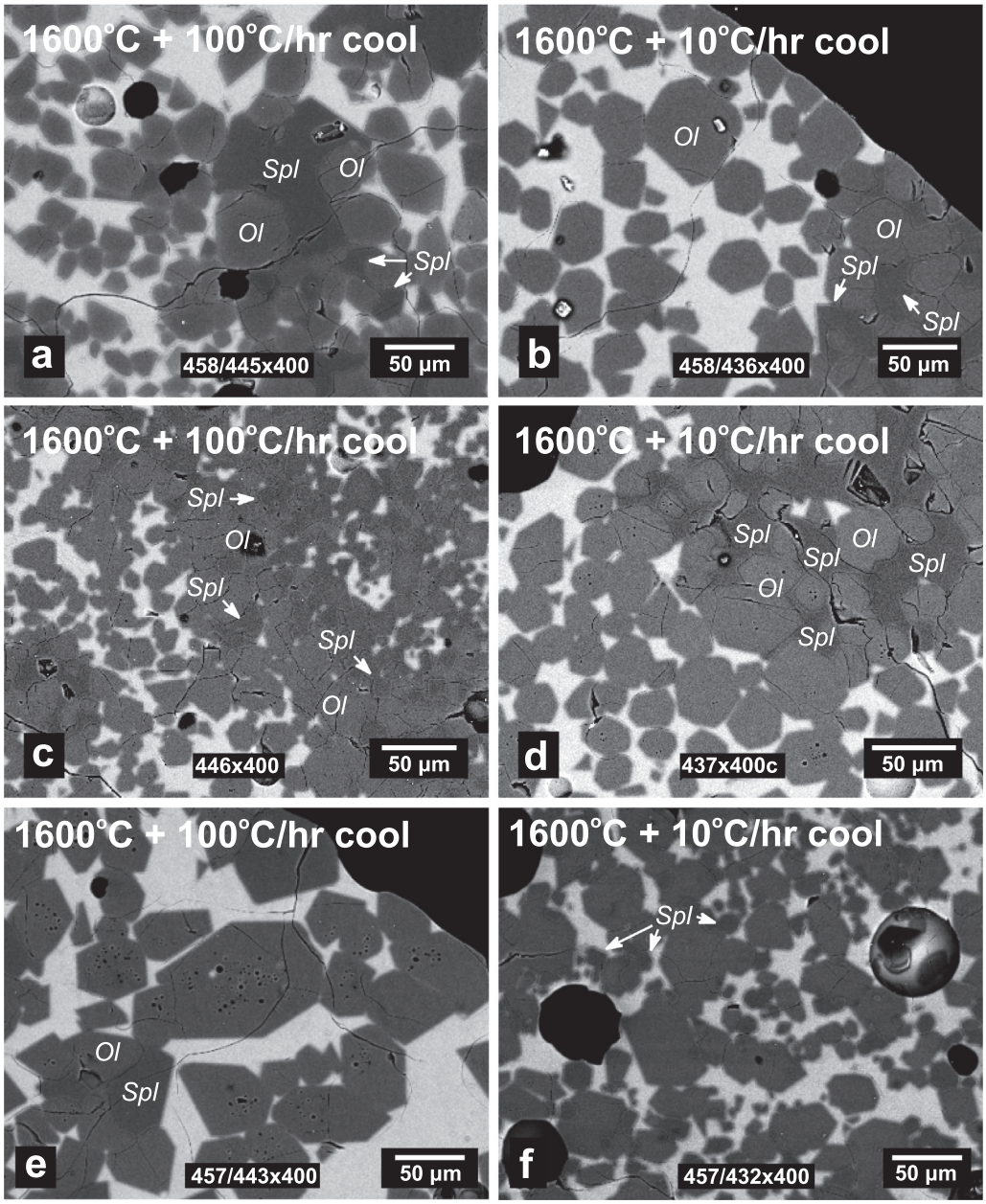

Fig. 5. SEM BSE images showing textures of charges from 100 °C/hour and 10 °C/hour dynamic crystallization runs. Synthetic (a, b) CAI + SCO, (c, d) CAI + Fo gel, (e, f) AOA. Note spinel partly enclosing olivine. Abbreviations Ol olivine, Spl spinel.

in concentrations of SiO_2, Al_2O_3, FeO, MgO and CaO in phases comprising our CAI + SCO and AOA isothermal and dynamic crystallization runs. Changes of the melt composition are complex because of the heterogeneity of the charges, with slow dissolution of spinel and olivine in the different parts during heating. Fig. 8 shows changes in olivine composition.

The principal compositional differences between the starting materials of the CAI + SCO and AOA runs are the lower Al and higher Fe in the former (Table 1) because the AOA has a higher CAI fraction (35% vs. 20%), and olivine is Fo_{100} rather than SCO (Fo_{88} with 11.35 wt% FeO). Nonetheless, comparison of images in Fig. 5 and trends in Fig. 7 shows that these differences had no effect on igneous textures, except that AOA is more completely melted at 1600 °C. There is little effect on ultimate compositional evolution, except for enrichment of liquid in Fe as olivine melts and a consequent dilution of other components. We show the resulting mesostasis and olivine compositions in Figs. 7 and 8, respectively. As the details are a little simpler for the AOA runs, we discuss only CAI + SCO compositions in detail below.

3.3.1. Mesostasis in SCO + synthetic CAI runs

The initial massive synthetic CAI has SiO_2 (41–46 wt%), Al_2O_3 (34–-37 wt%), and CaO (18–-20%) concentrations at

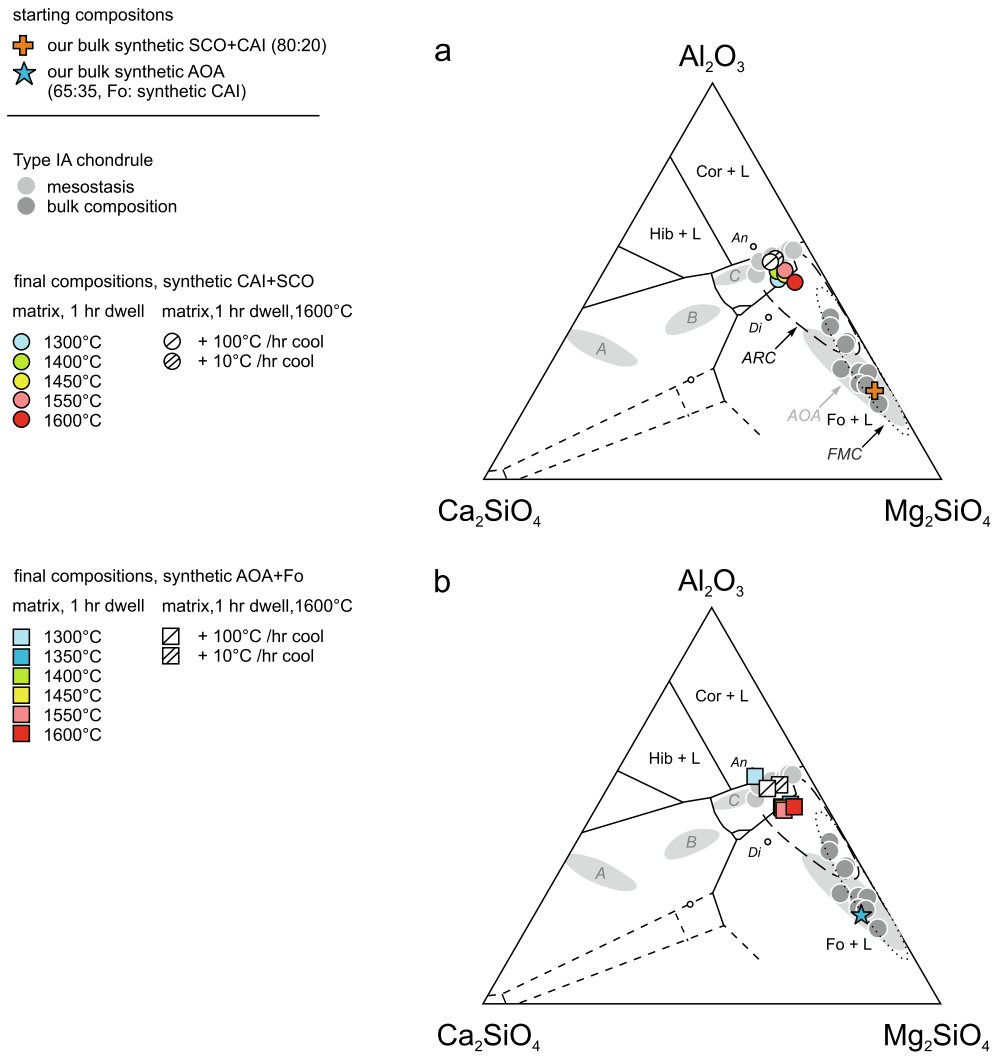

Fig. 6. Mean matrix/mesostasis compositions of 1 h isothermal charges plus runs heated for 1 hour at 1600 °C and cooled at 100 °C/hour and 10 °C/hour projected from $MgAl_2O_4$ (spinel) onto the plane Ca_2SiO_4 (larnite)–Mg_2SiO_4 (forsterite)-Al_2O_3 (corundum). Chondrule points, CAI data, and field boundaries as for Fig. 1. Abbreviations: An, anorthite; Cor, corundum; Di, diopside; Fo, forsterite; Sp, spinel; and L, liquid (melt).

1250 °C (Fig. 7) with traces of Fe and Mg, i.e., it is mostly anorthite probably with an intergranular film of glass. At 1300 °C, as mainly diopside and anorthite in the CAI lumps are being melted, the liquid is enriched in Si, Mg, and Ca relative to the CAI component. Anorthite largely survives at 1300 °C, as do spinel and olivine. FeO and MgO increase from initial Type C CAI concentrations of ~0.5 and ~1–3 wt% at 1250 °C, respectively, to about 4–6 wt% and ~12–-15 wt%, respectively in the glass fraction at 1300 °C.

At 1300 °C, mesostasis contains 45 wt% SiO_2. At higher temperature and as spinel melts progressively, SiO_2 in the mesostasis decreases to 34–37 wt% and Al_2O_3 content steadily increases from a concentration of ~20% at 1300 °C to a maximum of ~31 wt%, overlapping both the Type C CAI and Type IA chondrule mesostasis fields (Fig. 7). CaO steadily decreases from 14–16 wt% at 1300 °C to a minimum of between ~7–-9.5 wt% at 1600 °C. However, there is great heterogeneity in mesostasis compositions at 1450 °C (9–21 wt% MgO) due to the partly mixed interstitial liquid(s). As the SCO and spinel partly melted, FeO and MgO in the mesostasis increase, reaching maxima of ~10–11 wt% and 13–18 wt%, respectively at 1600 °C.

In dynamic crystallization runs cooled at 100 °C/h and 10 °C/h after a 1 h dwell at 1600 °C, olivine and spinel crystallization yields a fractionated mesostasis. This mesostasis records ~46–49 wt% and ~52–54 wt% SiO_2, ~21.5–24 wt% and 24–26 wt% Al_2O_3, 16–17 wt% and 14.5–16 wt% CaO, 5–7 wt% and 1.5–2 wt % FeO, and ~5 wt% and 7 wt% MgO, respectively, after having cooled at 100 °C/h and 10 °C/h (Fig. 7). These compositions are within the range of Type IA chondrule mesostasis.

3.3.2. Olivine and spinel in SCO + synthetic CAI runs

Olivine FeO content in synthetic CAI + SCO runs is closest (Fa_{5-10}, Fig. 8) to the original San Carlos ($Fa_{11.6}$) in the massive olivine at low temperatures (1250–1300 °C)

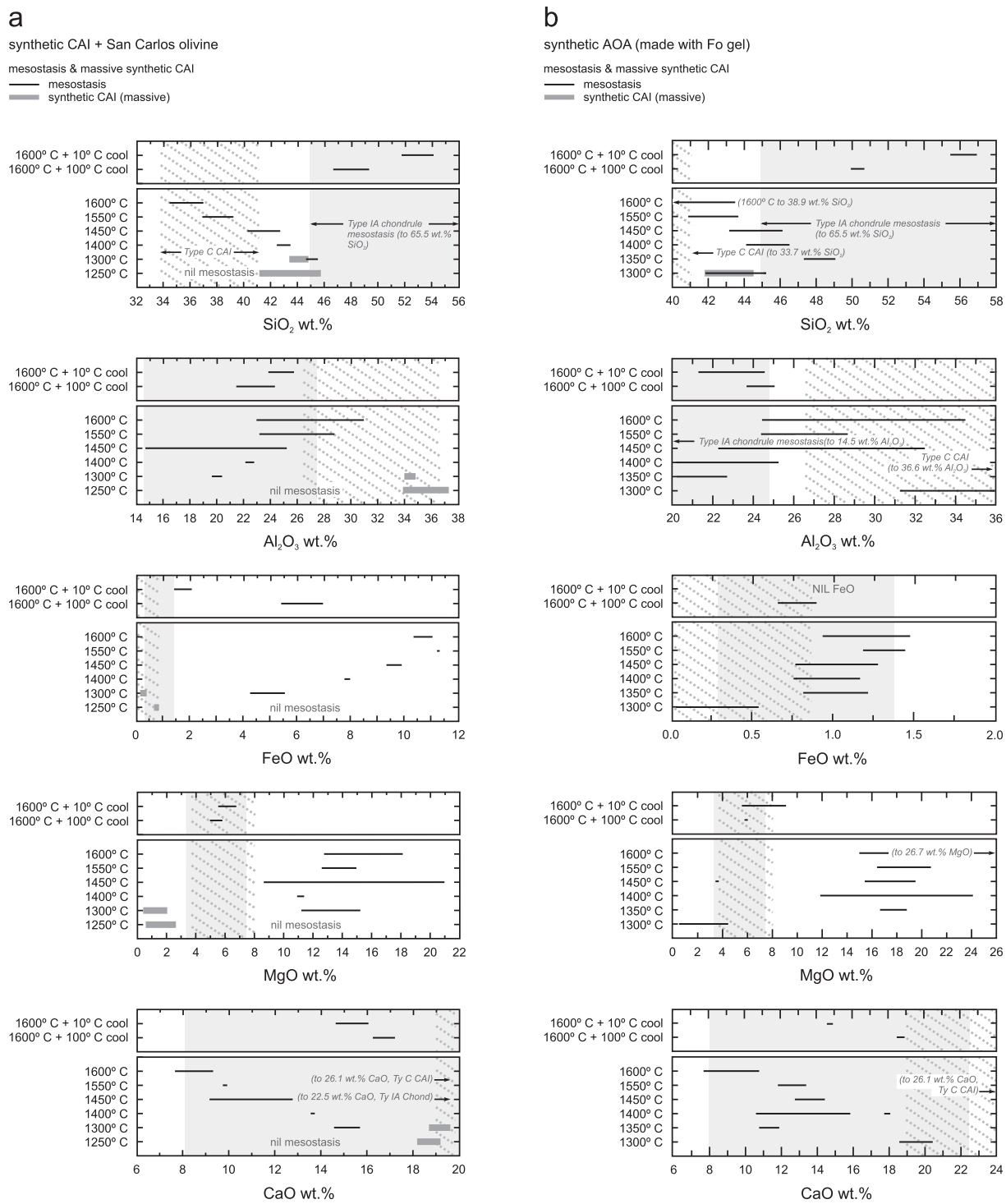

Fig. 7. Compositional changes with temperature in isothermal and dynamic crystallization runs of the synthetic (a) SCO + CAI and (b) AOA charges compared with natural Type IA chondrules and Type C CAI. Type IA chondrule mesostasis compositions are from Jones and Scott (1989). Type C CAI compositions are from Beckett (1986) and Wark (1987). Massive refers to large (>200 μm) forsterite masses (see Fig. 3a, 4a). Type I chondrule mesostasis compositions from Ichikawa and Ikeda (1995, Yamato (Y-8449) CR chondrite), Krot et al. (2004a,b, CR chondrites), Libourel et al. (2006, Semarkona LL3.0 chondrite and CR2 chondrite) and Kimura et al. (2020, Asuka 12,169 CM chondrite) have similar compositions (not shown) except that SiO_2 is significantly higher and Al_2O_3, FeO, MgO and CaO are lower in Y-8449 than for Semarkona.

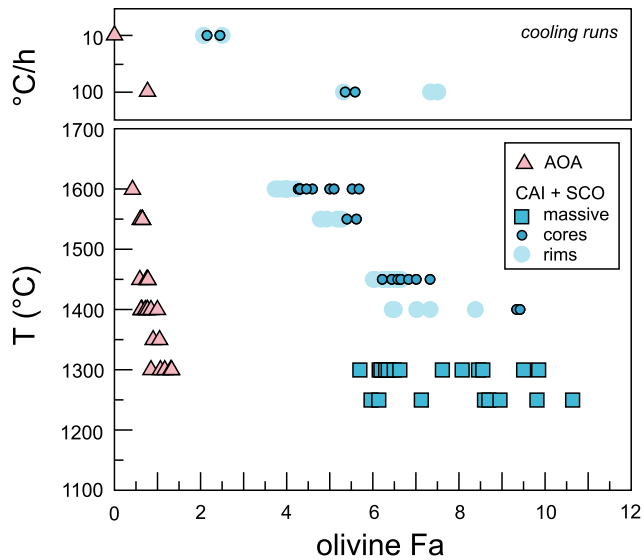

Fig. 8. Olivine composition for synthetic CAI-SCO and AOA compositions for isothermal experiments and dynamic crystallization experiments. Massive refers to large (>200 μm) forsterite masses (see Fig. 3a, 4a) and cores and rims refer to the cores and rims of small (~10–60 um) discrete forsterite grains (see Fig. 3c-f, 4c-f), respectively.

but has obviously already contributed some iron to the melt (Fig. 7). At higher temperatures in the isothermal runs (1400–1600 °C), FeO concentrations in olivine decrease steadily and crystals are reversely zoned: crystal rims always record lower FeO than their cores (Fig. 8), due to dissolution and minor reduction: the reverse zoning and some kamacite inclusions are seen in cores (Fig. 3). In the isothermal runs, a minimum FeO is recorded at 1600 °C with olivine cores $Fa_{4.3-5.7}$ and rims $Fa_{3.7-4.1}$.

Upon cooling at 100 °C /hr from 1600 °C, olivine is normally zoned with cores of $Fa_{5.5}$ and rims up to $Fa_{7.5}$. Cooling at 10 °C /hr yields the most magnesian olivine of all runs ($Fa_{2.1-2.5}$), because of the much longer duration at high temperature. This decrease in FeO with increasing temperature is consistent with a steady change from Type IIA-like and San Carlos olivine, to ultimately Type IA chondrule olivine upon cooling at 10 °C/hr.

The discrete olivine crystals in the 1400–1600 °C isothermal runs contain ~0.1–0.4 wt% CaO similar to olivine in Type IA chondrules, and ~0.3–0.4 wt% Al_2O_3, also levels similar to those of olivine in AOA (e.g., Komatsu et al., 2009). The least ferroan olivine in the CAI-SCO runs is relict and very close to the initial San Carlos composition. Olivine incorporates Ca at AOA levels as it loses Fe on dissolution. Some higher CaO and Al_2O_3 concentrations in the low temperature massive olivine appear to be due to overlap on tiny glass pockets. Similarly skeletal olivine grains in 1600 °C runs record a wide range of apparent Ca and Al concentrations probably due to intergrown glass within the skeletal grains.

Spinel in isothermal experiments is stoichiometric, and in the SCO + CAI runs, contains 3–4% FeO. In the 100 °C/h cooling run, it contains ~3.8–5.2 wt% FeO and in the 10 °C/h cooling run, about 1.6–2 wt% FeO.

3.3.3. Phase compositions in synthetic AOA runs

At temperatures up to 1350 °C, SiO_2 concentrations in the matrix of the AOA runs increase relative to their CAI inclusions, due to melting of diopside and anorthite. At higher temperatures, however, SiO_2 in mesostasis decreases to about 41–44 wt% at 1600 °C (Fig. 7) as forsterite melts. In the dynamic crystallization runs, SiO_2 contents rise steeply to 50–51 wt% after 100 °C/h cooling and 55–57 wt% SiO_2 after 10 °C/h cooling, due to the failure of diopside and anorthite to crystallize after forsterite and spinel. The mesostasis compositions plot in the field of Type IA chondrule mesostasis (Fig. 6). The forsterite we used was Fe- and Ca-free. In the isothermal runs it acquired Fe from the melt (Fig. 8). It also took up Ca at levels similar to those of olivine in AOA (e.g., Komatsu et al., 2009).

4. DISCUSSION

4.1. Cai and AOA as precursors for chondrules

Refractory inclusions are of wide interest as they provide clues regarding the some of the hottest environments known to have existed within the solar nebula. Natural fine-grained spinel-rich CAI and AOA are distinct from each other, with the former comprising a sintered assemblage of anorthite, diopside and spinel and AOA consisting of forsteritic olivine, kamacite, and discrete CAI bodies composed of Al-diopside, spinel, ±anorthite, ± melilite (Fig. 2). They have been investigated in many chondrite classes, e.g., CR, CV, CM, CO, CH, CB, and ungrouped carbonaceous chondrites Acfer 094, Adelaide, and Lewis Cliff (LEW) 85,332 (Krot et al., 2004a). As the minerals of AOA are similar to those which commonly occupy rims of CAI, they are probably coeval and formed close to one

Table 3
Composition of materials of the synthetic CAI + SCO (mixed as 20:80) charges subjected to isothermal and dynamic crystallization runs.

	Mesostasis	*n*	Massive CAI	*n*	Massive olivine	*n*	Olivine core	*n*	Olivine rim	*n*	Skeletal olivine	*n*	Relic spinel	*n*	Ophitic spinel	*n*
1250 °C																
oxide wt%																
SiO_2			41.10–45.70	3	40.87–42.16	8							*0.13–3.19*	6		
TiO_2																
Al_2O_3			33.88–37.30	3									66.73–69.74	6		
FeO			0.71	1	5.92–10.32	8							4.14–4.48	5		
Cr_2O_3																
MnO																
MgO			0.58–2.63	3	48.46–52.51	8							24.25–26.14	6		
CaO			18.16–19.19	3	0.13–0.82	6							0.16–1.08	5		
Na_2O			0.14–0.20	2												
1300 °C																
oxide wt%																
SiO_2	44.60–45.46	4	43.34–44.77	6	40.67–42.1	15							*0.27*	1		
TiO_2	0.21	1														
Al_2O_3	19.6–20.33	4	34.96–35.60	6	*1.31*	1							69.24–70.40	6		
FeO	4.23–5.52	4	0.24–0.49	3	5.69–9.46								3.35–3.73	6		
Cr_2O_3																
MnO																
MgO	11.19–15.21	4	0.40–2.03	6	48.55–52.79	15							25.72–26.79	6		
CaO	14.59–15.68	4	18.67–19.60	6	0.17–1.07	12							0.12	1		
Na_2O																
1400 °C																
oxide wt%																
SiO_2	42.42–43.43	2					40.52–40.92	2	40.84–42.23	5						
TiO_2	0.19	1														
Al_2O_3	22.09–22.75	2											69.37–69.60	2		
FeO	7.74–7.95	2					8.99–9.13	2	6.40–8.14	5			3.37–3.85	2		
Cr_2O_3																
MnO									0.21	1						
MgO	10.91–11.37	2					48.93–49.17	2	49.95–52.44	5			26.36–26.62	2		
CaO	13.54–13.69	2					0.14–0.17	2	0.22–0.33	5						
Na_2O																
1450 °C																
oxide wt%																
SiO_2	40.25–42.64	6					40.92–41.94	8	40.87–41.84	12						
TiO_2	0.21–0.24	3														
Al_2O_3	14.69–25.16	6					*0.33*	1	*0.32–0.34*	2			68.77–70.87	5		
FeO	9.31–9.85	6					6.15–7.14	8	5.91–6.54	12			3.26–3.89	5		

(*continued on next page*)

Table 3 (*continued*)

	Mesostasis	*n*	Massive CAI	*n*	Massive olivine	*n*	Olivine core	*n*	Olivine rim	*n*	Skeletal olivine	*n*	Relic spinel	*n*	Ophitic spinel	*n*
Cr_2O_3																
MnO																
MgO	8.62–20.95	6					50.62–51.86	8	50.95–52.03	12			26.12–26.73	5		
CaO	9.14–12.74	6					0.16–0.38	8	0.26–0.42	12						
Na_2O																
1550 °C																
oxide wt%																
SiO_2	36.87–39.18	2					41.51–41.63	2	41.42–41.96	4			*0.32–0.36*	2		
TiO_2	0.22	1														
Al_2O_3	23.14–28.73	2					*0.40–0.48*	2	*0.36–0.59*	3			68.88–69.74	8		
FeO	11.22–11.29	2					5.27–5.49	2	4.67–5.17	4			3.03–3.53	8		
Cr_2O_3																
MnO																
MgO	12.57–14.94	2					51.59–51.73	2	52.05–52.40	4			25.89–26.52	8		
CaO	9.72–9.89	2					0.15–0.21	2	0.19–0.39	4						
Na_2O																
1600 °C																
													nil			
oxide wt%																
SiO_2	34.42–36.94	3					40.84–42.12	10	40.87–41.99	10	39.69–41.31	9				
TiO_2																
Al_2O_3	22.93–30.92	3					*0.37–0.47*	7	*0.31–2.04*	10	*1.16–4.39*	9				
FeO	10.32–10.99	3					4.16–5.49	10	3.61–4.09	10	4.29–6.79	9				
Cr_2O_3																
MnO	0.21	1														
MgO	12.74–18.10	3					51.30–53.64	10	51.63–53.84	10	48.49–52.55	9				
CaO	7.64–9.29	3					0.13–0.26	9	0.15–0.26	9	0.24–1.05	9				
Na_2O																
1600 °C + 100 °C/hour cool																
													nil			
oxide wt%																
SiO_2	46.62–49.28	5					42.60–42.72	2	41.33–42.98	3						
TiO_2	0.42	1														
Al_2O_3	21.43–24.31	5													69.20–69.96	4
FeO	5.38–6.94	5					5.47–5.81	2	5.45–7.55	3					3.83–5.21	4
Cr_2O_3															0.40	1
MnO																
MgO	4.96–5.78	5					54.24–55.02	2	51.78–54.46	3					26.22–26.94	4

Table 3 (*continued*)

	Mesostasis	*n*	Massive CAI	*n*	Massive olivine	*n*	Olivine core	*n*	Olivine rim	*n*	Skeletal olivine	*n*	Relic spinel	*n*	Ophitic spinel	*n*
CaO	16.24–17.19	5					0.28	1	0.27–0.30	2						
Na_2O																
1600 °C + 10 °C/hour cool													nil			
oxide wt%																
SiO_2	51.71–54.08	9					41.79–42.75	2	42.01–42.69	3						
TiO_2																
Al_2O_3	23.81–25.69	9													69.35–70.12	2
FeO	1.43–2.05	9					2.22–2.48	2	2.10–2.54	3					1.64–2.01	2
Cr_2O_3																
MnO																
MgO	5.52–6.74	9					55.47–56.56	2	55.68–56.64	3					27.94–28.10	2
CaO	14.62–16.04	9					0.28	1								
Na_2O																

Note: Isothermal runs are of 1 h soak time and dynamic crystallization runs are preceded by 1 h soak time (at 1600 °C).
For analyzes in italics, see explanation in text.
Abbreviations: SCO = (crushed) San Carlos olivine.
Data taken form Soak IPR data.

another in time and space (see review of Krot et al., 2009). There also exists evidence suggesting that chondrules, particularly Al-rich chondrules, and CAI are genetically related (e.g., Krot and Rubin, 1994; Russell et al., 2000; Krot and Keil, 2002; MacPherson and Huss, 2005; Krot et al., 2006a,b).

The dust ball model of chondrule formation describes the heating and consequent partial melting of precursor agglomerates of grains, generally as closed systems, in the innermost regions of the protoplanetary disk (Nagahara and Kushiro, 1982; Taylor et al., 1983; Grossman, 1988; Hewins, 1997; Jones et al., 2005). It is clear now that many chondrules evolved while molten by interaction with dense gas (Tissandier et al., 2002; Nagahara et al., 2005; Krot et al., 2006a,b; Libourel et al., 2006; Schrader et al., 2013; Tenner et al., 2015; Villeneuve et al., 2015; Piralla et al., 2021) or even formed as condensed liquids (Varela et al., 2006; Engler et al., 2007), and we discuss implications of this below. Nevertheless, the origin of the initial dust grains and the relationship between RI and chondrules remains an important problem. Al-rich chondrules (ARC, Bischoff and Keil, 1983a,b, 1984; Bischoff et al., 1985; Bischoff et al., 1989; MacPherson and Huss, 2005; Tronche et al., 2007) which have chemical compositions intermediate to those of ferromagnesian chondrules and plagioclase-rich CAI (MacPherson and Huss, 2005), appear to have contained a small proportion of CAI-like refractory constituents in their precursor materials. Other evidence of a genetic relationship between some chondrules and CAI is preserved in trace element compositions. For example, some chondrules retain a fractionation signature by virtue of positive anomalies in some REE (Ce, Yb) and display robust REE fractionation patterns akin to those of Group II CAI (Misawa and Nakamura, 1988). These observations require that CAI were present in the chondrule-forming regions when chondrules formed. Indeed, relict CAI have been found in plagioclase-rich chondrules in CR, CH, and reduced CV chondrites (Krot and Keil, 2002; Krot et al., 2002).

Krot et al. (2004a,b) demonstrated that the texture and bulk composition of some AOA are chemically similar to magnesian chondrules, and thus may provide a possible genetic link between CAI and chondrules. The numerous examples of AOA enclosed within Mg-rich chondrules (Nagahara and Kushiro, 1982; Misawa and Nakamura, 1996; Komatsu et al., 2001; Scott and Krot, 2003; Krot et al., 2005; Krot et al., 2017; Marrocchi et al., 2019a) are consistent with AOA precursors for chondrules. Zhang et al. (2020) also concluded that some ARC are the result of melting of both AOA and Types B and C CAI precursors. Thus, a strong case has been made that some magnesian chondrule precursors were AOA-like fine-grained nebular condensates. Alternatively, precursors might also have been granoblastic olivine aggregates (GOA) (Hewins and Fox, 2004; Libourel and Krot, 2007). However, sintering experiments showed that GOA could be produced from sintering of fine-grained olivine aggregates like dustballs (Whattam et al., 2008; Whattam and Hewins, 2009), and addition of a small amount of plagioclase to such charges would have produced a mesostasis like those in chondrules.

Thus, GOA could themselves be derived from thermally annealed AOA. In such a scenario, many chondrule 'phenocryst' cores could be relict grains derived from GOA or AOA, rather than crystallized from the melt. Textural and isotopic properties found in OC chondrule olivine grains are similar to those in CC, consistent with AOA precursors (e.g., Piralla et al., 2021). The role of spinel relicts and O and other isotope variations supporting this interpretation are discussed in Sections 4.3 and 4.4.

4.2. Constraints on the formation conditions of RI and chondrules

The minerals of CAI (e.g., MacPherson et al., 2005; MacPherson, 2003) are stable at temperatures above the forsterite condensation point under canonical nebular conditions. AOA minerals on the other hand, consist of those predicted to follow forsterite (Grossman, 1972; Weisberg et al., 2004; Krot et al., 2009). AOA are therefore interpreted as products of more extensive condensation than for CAI that have accreted together and been sintered (Komatsu et al., 2001), but only in rare cases partly melted. Spinel forms by condensation of nebular gas after the Ca-Al oxide phases. Ebel (2006) reviewed publications of condensation calculations for different pressures, and found that the onset of spinel condensation occurs between 1245 and 1100 °C (sic), with the condensation temperatures decreasing with lower gas pressure. Olivine condensation follows in all cases after a drop of 50–70 °C, with diopside near the olivine temperature and with anorthite generally at lower temperatures. Laboratory condensation experiments found spinel forming at 1285 °C (Toppani et al., 2006) along with corundum, suggesting kinetic effects, and forsterite appearing at 1125 °C.

The temperatures required to melt CAI and AOA are much higher than those of condensation. Stolper (1982) crystallized spinel on the liquidus of a Type B CAI composition at 1550 °C, though CAI may not have been totally melted. A Type C CAI composition has a liquidus temperature of 1470 °C with spinel as the first solid phase (Tronche et al., 2007). CAI have much lower liquidus temperatures than Mg-rich chondrules (Stolper, 1982; Hewins et al., 2005) at ~1750 °C (e.g., Table 1), and are thus likely to be destroyed by melting during chondrule formation. The phase the most resistant to melting in natural CAI is spinel, stable at 1550 °C (Stolper, 1982), and it survives to 1550 °C in our AOA experiments. Indeed, in some igneous CAI it appears to be a relic of an earlier stage, probably formed by condensation (Aléon, 2018). AOA, on the other hand, have very similar liquidus temperatures to Type IA chondrules (Table 1). This results in many relict olivine grains in experiments heating spinel-free GOA (Whattam and Hewins, 2009) to 1550 °C, as with the present work on spinel-bearing AOA analogs.

Our sintering experiments described above focused on spinel-anorthite-diopside CAI compositions and, with added olivine, AOA compositions. They indicate that natural fine-grained spinel-rich CAI could have been produced with 100 h heating at 1200 °C, roughly at their condensation temperatures (Ebel, 2006). The sintered texture of natural AOA was reproduced with 200 h duration heating at 1250 °C of an assemblage of a CAI component with olivine.

In isothermal melting experiments, CAI inclusions in our CAI-olivine AOA charges begin to melt at ~1300 °C, as also observed for an anorthite-olivine-melilite AOA analog (Komatsu et al., 2001). For all three starting mixtures, the mesostases are generally dissimilar to Type IA chondrule mesostasis and similar to Type C CAI mesostasis. Pure CAI would be expected to melt completely at ~1550 °C (Stolper, 1982). The mesostasis composition of the AOA charges evolves, with Al and Fe increasing at higher temperatures, due to dissolution of spinel and, where present, SCO. By 1400 °C there is a connecting mesostasis to the two domains, olivine-bearing and Ca-Al-rich, the latter being recognized as clusters of spinel relict grains in glass (Fig. 3). In such charges the continuous interstitial glass is very variable in composition. Melt Al and Fe concentrations increase as spinel and olivine dissolve. By 1600 °C, spinel has disappeared, leaving no traces of the CAI component. This suggests that PO chondrules with relict spinel could have had peak temperatures up to 1550 °C but temperatures higher than this would have erased this evidence of a CAI or AOA precursor. The overall effect of melting of AOA-like materials at higher temperature is production of olivine 'porphyry' though cores of some olivine 'phenocrysts' are partly modified San Carlos relicts (Fig. 3). In the CAI + SCO runs, the high FeO content of the olivine and the high degree of melting give more magnesian olivine (Fig. 8) and mesostasis that is more ferroan than Type IA chondrule mesostasis (Fig. 7). Though spinel relicts are relatively widespread in chondrules (Komatsu et al., 2001; Maruyama and Yurimoto, 2003; Tenner et al., 2017; Marrocchi et al., 2019a), chondrules with two domains, olivine-rich and Ca-Al-rich are not. Excluding condensation of chondrule and RI precursors, this indicates two distinct types of events: sintering and agglomeration of RI (and possibly of Fo chondrule precursors into granoblastic olivine aggregates (GOA, see Whattam et al., 2008; Whattam and Hewins, 2009) followed by melting, rather than heating of dust at a continuum of temperatures. Pristine (unmelted) RI therefore did not survive in domains where chondrules formed and they record the conditions of condensation, whereas the chondrules document conditions experienced in subsequent events and reservoirs.

In the cooling rate runs the mesostasis compositions are akin to those of Type IA chondrules (Figs. 6, 7) and identical to those of ARC (Fig. 8), particularly because diopside and anorthite failed to crystallize. The charges contain at least 50% olivine at 1600 °C (Fig. 3f) as relict grains. An interesting feature of these dynamic crystallization experiments was that spinel crystallized during cooling at 10 °C/h and 100 °C/h, and is interstitial to and ophitically enclosing olivine (Figs. 3, 4). Aluminous low-Cr spinels in Allende ferromagnesian chondrules have been interpreted as having formed in-situ rather than as relict grains (Ma et al., 2008). Some plagioclase-rich chondrules with CAI relicts appear to contain incompletely homogenized melts (Krot et al., 2002). A heterogeneous distribution of melt, e.g., due to clustering of olivine, followed by introduction

Table 4
Composition of materials of the synthetic AOA + Fo (mixed as 35:65) charges subjected to isothermal and dynamic crystallization runs.

	Mesostasis	*n*	Massive CAI	*n*	Olivine	*n*	Relic spinel	*n*	Ophitic spinel	*n*
1300 °C										
oxide wt%										
SiO_2	41.80–45.23	15	41.80–44.52	6	41.62–44.06	5	0.18	1		
TiO_2							0.27			
Al_2O_3	31.26–35.98	15	31.26–35.86	6			70.48	1		
FeO			0.03–0.53	6	0.89–1.34	5	0.96			
Cr_2O_3										
MnO										
MgO	0.53–4.53	15	0.55–4.53	6	54.67–58.36	5	27.92	1		
CaO	16.82–20.47	15	16.82–19.29	6			0.06	1		
Na_2O	0.01–0.02	3	0.01–0.02	2						
1350 °C										
oxide wt%										
SiO_2	47.33–49.09	14			41.95–42.97	2	0.12–0.62	5		
TiO_2					0.01	1	0.01–0.12	5		
Al_2O_3	21.04–22.72	14					71.00–71.36	5		
FeO	0.81–1.21	14			0.94–1.05	2	0.64–0.94	5		
Cr_2O_3										
MnO										
MgO	15.98–18.83	14			55.66–58	2	27.20–27.48	5		
CaO	10.88–11.94	10			0.14–0.30	2	0.05–0.14	5		
Na_2O	0.01–0.03	2					0.02	2		
1400 °C										
oxide wt%										
SiO_2	44.09–46.51	15			41.99–43.74	8	0.10–0.14	3		
TiO_2										
Al_2O_3	20.20–25.27	15			0.08–1.57	4	71.03–71.14	3		
FeO	0.74–1.16	15			0.64–1.05	8	0.64	3		
Cr_2O_3										
MnO					0.01–0.04	3	0.01–0.03	3		
MgO	11.86–24.14	15			55.26–58.64	8	27.29–27.65	3		
CaO	10.62–15.89	15			0.20–0.28	4	0.04–0.06	3		
Na_2O	0.01–0.05	4					0.02	2		
1450 °C										
oxide wt%										
SiO_2	43.17–46.13	13	44.41	1	42.26–43.50	4	0.06–0.12	3		
TiO_2					0.04–0.08	2				
Al_2O_3	22.29–24.85	13	32.50				70.67–71.30	5		
FeO	0.96–1.27	13	0.76		0.61–0.78	4	0.73–0.94	5		
Cr_2O_3										
MnO					0.02–0.04	2				

(*continued on next page*)

Table 4 (*continued*)

	Mesostasis	*n*	Massive CAI	*n*	Olivine	*n*	Relic spinel	*n*	Ophitic spinel	*n*
MgO	15.49–19.58	13	3.59		55.40–57.74	4	27.32–27.48	2		
CaO	12.81–14.47	13	17.94		0.21–0.31	3	0.04–0.05	3		
Na_2O			0.16							
1550 °C										
oxide wt%										
SiO_2	40.86–43.68	9			42.05–43.73	5	0.06–0.12	5		
TiO_2					0.02	1	0.19–0.24	5		
Al_2O_3	24.41–28.69	9			0.24–0.37	3	72.10–72.82	5		
FeO	1.17–1.44	9			0.61–0.69	5	0.63–0.84	5		
Cr_2O_3										
MnO										
MgO	15.80–20.73	9			55.71–58.97	5	27.42–27.61	5		
CaO	11.86–13.43	9			0.24–0.35	5	0.02–0.06	5		
Na_2O	0.02–0.06	2								
1600 °C										
							nil			
oxide wt%										
SiO_2	38.99–43.49	19			41.57–41.84	2	0.11–0.36	3		
TiO_2							0.04–0.13	3		
Al_2O_3	24.45–34.50	19			0.50–0.53	2	71.20–72.24	3		
FeO	0.93–1.47	19			0.42–0.45	2	0.30–0.69	3		
Cr_2O_3										
MnO										
MgO	15.03–26.57	19			56.07–56.50	2	27.55–28.01	3		
CaO	7.77–10.85	19			0.20–0.22	2	0.04–0.05	3		
Na_2O										
1600 °C + 100 °C/hour cool										
							nil			
oxide wt%										
SiO_2	49.92–50.67	5			43.30	1				2
TiO_2										
Al_2O_3	23.68–25.07	5							69.52–71.69	2
FeO	0.65–0.89	5			0.80	1			0.53–0.74	2
Cr_2O_3										
MnO										
MgO	5.82–6.09	5			57.69	1			28.82–29.42	2
CaO	18.47–18.91	5			0.46	1				

(*continued on next page*)

Table 4 (*continued*)

	Mesostasis	*n*	Massive CAI	*n*	Olivine	*n*	Relic spinel	*n*	Ophitic spinel	*n*
Na_2O										
1600 °C + 10 °C/hour cool							nil			
oxide wt%										
SiO_2	55.45–56.93	7			42.94	1				
TiO_2										
Al_2O_3	21.30–24.58	7							70.9	1
FeO										
Cr_2O_3										
MnO										
MgO	5.57–9.12	7			58.33	1			29.66	1
CaO	14.56–14.90	7			0.25	1				
Na_2O										

Note: Isothermal runs are of 1 h soak time and dynamic crystallization runs are preceded by 1 h soak time (at 1600 °C).
For analyzes in italics, see explanation in text.
Data taken form Soak IPR data.

of Al-rich liquid from melted CAI patches during cooling, might also have contributed to the formation of interstitial spinel in the cooling rate runs and such chondrules. However, a simpler explanation is that our charges are more Al-rich than most Type I chondrules (Jones and Scott, 1989) and could have had spinel on the liquid line of descent.

4.3. Chondrule phase compositions and nebular reservoirs

Gas of chondritic or fractionated composition plays an extended role in the formation of components in chondrites, in the condensation of CAI (Grossman, 1972; Toppani et al., 2006), formation of accretionary forsterite rims on CAI and the formation of AOA (Krot et al., 2009), and conversion of olivine-rich aggregates (AOA or GOA) to chondrules (Jones et al., 2004; Whattam and Hewins, 2009; Marrocchi et al., 2018). Chondrule interactions with nebular gas include: incorporation of Mg into Ca-Al-rich melts to form outer olivine shells or palisades on chondrules (Nagahara et al., 2008; Libourel and Portail, 2018; Marrocchi et al., 2019a); incorporation of SiO to transform Type IA into Type IB chondrules by the formation of pyroxene (Tissandier et al., 2002; Libourel et al., 2006); and incorporation of SiO to oxidize and convert Type I into Type II chondrules (Villeneuve et al., 2015).

Many parameters relevant to chondrule formation are difficult to control simultaneously in experiments. In this study we have used a gas free of lithophile elements simply to control oxygen fugacity, giving us closed system melting and crystallization. Solid AOA inclusions in chondrules have yielded few signs of interaction with exterior gas, and our charges resemble many PO chondrules that have no outer shell modified by condensation. However, the best matches between our experimental charges and natural chondrules with relict spinel require heating to no higher than 1550 °C, rather than a temperature closer to the liquidus temperature (up to ~1800 °C, Hewins and Radomsky, 1990) of the bulk chondrule composition. This is a new constraint on the temperature of chondrule formation and is more consistent with models of olivine growth at sub-liquidus temperatures due to modification of RI melt droplets by Mg and SiO condensation from ambient gas than with closed-system chondrule formation. The fact that our olivine is unzoned, whereas chondrule olivine shows asymmetric zonation (Libourel and Portail, 2018; Marrocchi et al., 2019a), emphasizes the need for interaction between Mg- and SiO-bearing gas and natural chondrules. Similarly, our mesostasis compositions show variations resulting from the dissolution or crystallization of olivine, but such trends are absent from Type I chondrules where the liquid does not plot in the olivine stability field but is Ca-Al-rich like CAI (Libourel et al., 2006). This temperature is also the spinel disappearance and liquidus temperature of Type B CAI (Stolper, 1982).

In the closed-system model, the relatively Al-rich barred olivine (BO) chondrules are assumed to have formed at temperatures just above their liquidus temperatures. Hewins and Radomsky (1990) therefore took the range of

liquidus temperatures for BO chondrules, 1400–1750 °C, as typical chondrule formation temperatures, and this is consistent with the texture – liquidus relationship for porphyritic and non-porphyritic chondrules. In the open-system model, BO chondrules are inferred to have developed their bulk compositions by gas–melt interaction at ~1550 °C (Libourel and Portail, 2018) matching the CAI liquidus temperature and the spinel disappearance temperatures in our AOA experiments.

From this perspective, one could imagine chondrule formation immediately after initial nebular condensation of RI, if pressure had been high enough for liquid stability, as well as in subsequent extensive evaporation–condensa tion events. Despite dating of some individual chondrules suggesting formation contemporaneous with CAI formation (Connelly and Bizzarro, 2018) there is evidence from Al-Mg, Hf-W, and Pb-Pb systems that most chondrules formed 2–4 m.y. after the initial condensation (Kruijer et al. (2020). This supports the concept of distinct events with different peak temperatures.

Radiometric dating requires chondrule formation events after the initial formation of RI. One possible mechanism is the collision of large bodies (e.g., Hasegawa et al., 2016), that might involve melting, evaporation and recondensation. Chondrules in CB and CH chondrites show evidence for evaporation and condensation (in skeletal olivine chondrules and cryptocrystalline chondrules respectively, Hewins et al., 2018), dust-free accretion, and especially a "young" age (4.562--4.563 Ga; Bollard et al., 2015; Krot et al. 2005). These are characteristics of an impact plume setting. CBb chondrules also show evidence of partial remelting consistent with turbulence during rapid plume expansion (Hewins et al., 2018). Chondrules in other chondrites have textures more consistent with steady cooling and show sparse evidence for evaporation followed by recondensation, based on Na concentrations in olivine, melt inclusions and mesostasis, as well as ample evidence of condensation of Mg and SiO (Hewins and Zanda, 2012). Modeling shows that most collision-generated chondrules would have formed with the largest bodies, i.e., the final protoplanets (Hasegawa et al., 2016). The overwhelming evidence of condensation in "normal" chondrules suggests long term immersion in large impact plumes but rapid vapor dissipation for smaller collisions.

4.4. Chondrule isotopic compositions and nebular reservoirs

The oxygen isotopic composition of olivine in chondrules is an important tool used to explore the nature of precursors (e.g., Jones et al., 2004) and the evolution and spatial extent of chondrule-gas interactions (e.g., Tenner et al., 2018; Williams et al., 2020). In a pioneering study, Jones et al. (2004) reported two fine-grained (~20–50 μm) Type IA chondrules in the CV chondrite Mokoia showing very wide ranges of O isotopic compositions, with some grains having $\Delta^{17}O$ −25‰, like RI. Many subsequent authors (e.g., Schrader et al., 2013; Schrader et al., 2014) argued that Type IA chondrules and particularly their ^{16}O-enriched relict grains formed from AOA-like olivine. Schrader et al. (2018) also found $\Delta^{17}O$ of −25‰ for some olivine in accretional chondrules (resembling dark-zoned or protoporphyritic chondrules, Hewins et al., 1997) and they interpreted these grains as AOA material.

Jones et al. (2004) suggested that the O isotopic heterogeneity of chondrule olivine represents solid-state equilibration of relict grains, or incomplete gas–melt isotopic exchange during chondrule melting. Connolly and Huss (2010) argued that the Mg# and oxygen isotope composition of chondrules are related to the amount of dust and ice incorporated into the originally near-solar ambient gas. Schrader et al. (2013) and Schrader et al. (2014) assumed that CR Type I chondrules reacted with relatively ^{16}O-depleted gaseous H_2O and inferred the O-isotope composition of this reacting gas. For CO chondrites. Tenner et al. (2013) explained increasing Δ^{17} and $\Delta^{18}O$ in Type I olivine as primarily due to ice enrichment, and the FeO enrichment in Type II olivine as primarily due to dust enrichment in the gas. Tenner et al. (2015) quantified ice and dust enrichment factors for CR chondrites and argued that the snow line passed between the Type I and II reservoirs. Based on the present experiments and those of Whattam and Hewins (2009), we propose that gradual disaggregation of AOA precursor material yielded different durations of exposure to melt, the production of some relict grains, and hence different extents of O isotopic exchange for olivine grains in chondrules. However, heterogeneous dust aggregates are also possible precursors and Type II chondrules may have formed from Type I chondrule material (Connolly and Huss, 2010; Villeneuve et al., 2015).

Warren (2011) recognized a bimodality in stable isotope compositions that suggests a fundamental division between carbonaceous (CC) and non-carbonaceous (NC) meteorites, and suggested that these materials originally accreted in the outer solar system (CC) and inner solar system (NC). For AOA, Marrocchi et al. (2019b) found large, mass-dependent, light Si isotope enrichments that require rapid condensation over timescales of days to weeks. They concluded that such brief localized high-temperature events are inconsistent with disk transport timescales. Williams et al. (2020) supported the model of Tenner et al. (2015) of chondrule formation in gas reservoirs differentially enriched in dust and ice components and separation of chondrule types by a gap in the disc formed by Jupiter. Kruijer et al. (2020) indicated that this separation lasted between ~1 and ~4 My. Multi-isotope data for chondrules support separate reservoirs: no CC chondrules plot in the NC chondrite field, and no NC chondrules plot in the CC field (Schneider et al., 2020). They concluded that there was no disk-wide transport of chondrules or exchange between the NC and CC reservoirs. Though there were similar evaporation/recondensation processes and recycling for NC and CC chondrules Piralla et al. (2021) showed they are distinctly different in $\Delta^{18}O - \Delta^{17}O$ space indicating a lack of genetic relationship: this makes extensive radial transport implausible. However, some dusty olivine grains in CM chondrules have $\Delta^{17}O$ ~0‰ that match those of UOC chondrule olivine (Schrader et al., 2020), suggesting some limited migration from the inner to the outer solar system.

Spinel relicts occur in plagioclase-olivine inclusions, Type IA chondrules and barred-olivine (Sheng et al., 1991; Misawa and Fujita, 1994; Maruyama and Yurimoto, 2003; Tenner et al., 2017) in the Allende and C3.2ung chondrites. We have observed them in Semarkona (Hewins et al., 2012) and Paris chondrules, including Type IIA chondrules (Hewins et al., 2014). Because of slow oxygen diffusion (Ryerson and McKeegan, 1994), spinel tends to retain ^{18}O-poor compositions during reheating of RI, including relict CAI in chondrules with Δ^{17}O of ~−22‰ for spinel (e.g., Krot et al., 2006a,b). Maruyama and Yurimoto (2003) reported extremely ^{16}O-rich (Δ^{17}O −17‰) spinel in small grains in a plagioclase-rich chondrule. Tenner et al. (2017) reported spinel in an Al-rich chondrule with a Δ^{17}O value of −19‰ consistent with an origin in AOA. However, spinel with isotopic compositions consistent with chondrule values is also found (Rudraswami et al, 2011). Tracking olivine composition changes for all kinds of chondrites gives information on the changing compositions of nebular reservoirs and transport mechanisms (Schrader et al., 2020; Williams et al., 2020), but finding detailed evidence for such processes is labor-intensive, as summarized by Tenner et al. (2018). Analysis specifically of the less abundant spinel could be useful.

4.5. Conceptual model for spinel-bearing chondrule formation

In view of debate on exactly how RI and chondrules formed in isotopically distinct regions of the solar nebula, a key observation is that, though NC and CC chondrules are distinct in oxygen isotopic composition, each is accompanied by AOA of the appropriate Δ^{18}O and each varies in Δ^{17}O as a function of the amount of exchange with gas (Piralla et al., 2021). In Section 4.2, we summarized the temperature and time conditions required for the formation of RI and the transformation of RI into chondrules based on experiments of the present study. Using these data, we provide a conceptual model for the transformation of RI into chondrules in Fig. 9. Here we illustrate two steps, the

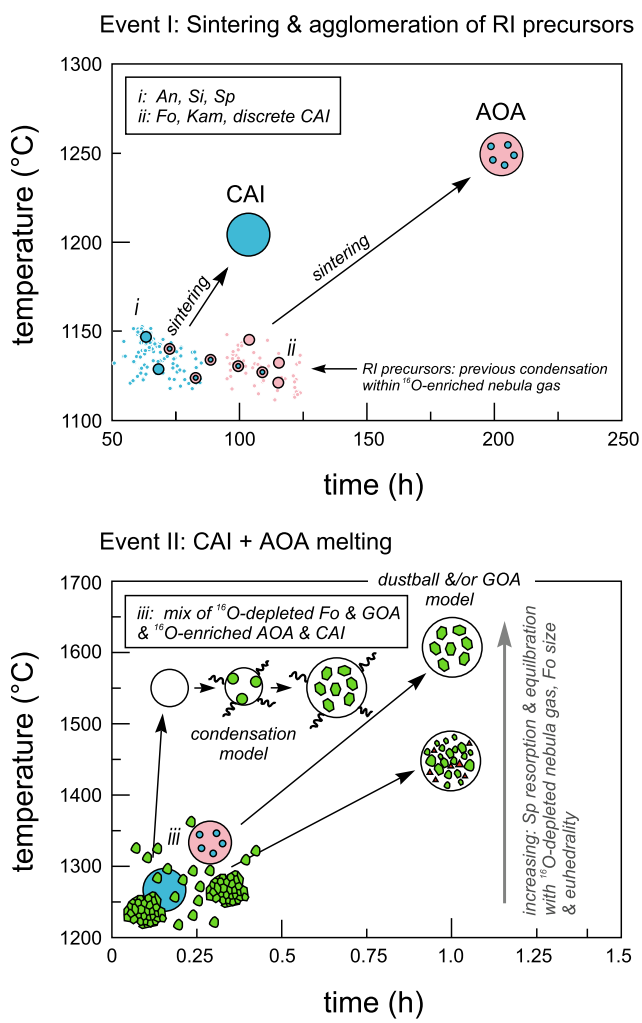

Fig. 9. Cartoon conceptualizing the formation of spinel-bearing chondrules. (1) Sintering of condensate dust to produce CAI and AOA. (2) Melting of CAI and AOA, with or without addition of Mg and Si from the gas to produce Type IA chondrules. Both CAI and AOA melted below 1550 °C could produce chondrules with relict spinel.

sintering of condensates into RI, with the incorporation of CAI and forsterite into AOA, followed by the partial melting of AOA to form chondrules. We also illustrate the idea that large reheated CAI could be transformed by interaction with gas to form chondrules. Libourel and Portail (2018) have argued that addition of Mg(g) and SiO(g) leads to Mg-rich olivine saturation in Ca-Al-rich melts and the crystallization of zoned olivine in Type IA chondrules. Marrocchi et al. (2018) observed relict olivine grains with refractory overgrowths formed from Ca-Al-rich melts during gas-assisted melting of nebular condensates like amoeboid olivine aggregates. In Fig. 9 we contrast two end-member models for chondrule formation by melting whole CAI or AOA-like materials.

Subsequent to condensation of precursors of RI and chondrules in isotopically distinct regions (^{16}O-enriched in the case of the former and ^{16}O-depleted in the latter), exposure of RI precursor condensates to solar nebular temperatures of 1200–1250 °C for at least 100––200 h resulted in production of sintered assemblages of AOA and CAI. Note that these time scales are the same as those indicated by Marrocchi et al. (2019b) for condensation to produce large Si mass fractionations in AOA. As AOA include discrete fragments of CAI, this suggests that AOA formed after CAI. A thermal event similar to that which resulted in sintering of RI may also have caused annealing of Fo condensates to form GOA (Whattam et al., 2008; Whattam and Hewins, 2009), though in the case of GOA, whereas heating times may have been similar to those of RI (>100 h), temperatures would have been much higher (>1500 °C). Subsequently, partial melting of chondrule precursors of Fo condensates and/or GOA in the presence of RI at maximum temperatures of 1550 °C resulted in chondrule formation and the interaction of RI spinel with ^{16}O-poor nebula gas. Due to the slow diffusion of oxygen in spinel (Ryerson and McKeegan, 1994), chondrule spinel retained ^{16}O compositions enriched relative to chondrule olivine and other phases. The isotopic composition and, as the experiments of the current study show, the volume of surviving spinel would reflect the temperature and hence degrees of partial melting that spinel was subject to. High degrees of partial melting would result in chondrules with less spinel with a more ^{18}O-rich composition more similar to that of chondrule olivine, while lower degrees of partial melting would yield more spinel with ^{16}O-equilibrated compositions. Another clue to the relative temperature that chondrule precursors were subjected to is the size and morphology of olivine which coarsens and becomes increasingly euhedral with increasing temperature (Whattam and Hewins, 2009).

In our experiments, partly melted AOA domains survive only at low temperatures, but in charges melted at temperatures yielding porphyritic textures, relict spinel is the main evidence of the former presence of AOA. This key observation suggests that spinel grains in chondrules are more likely to be derived from AOA than are olivine relicts, which could be derived from older chondrules. Therefore, studying specifically spinel-bearing chondrules could rapidly yield most valuable information on chondrule-gas exchange and potential transport.

5. CONCLUSIONS

(1) CAI and AOA textures can be reproduced by sintering at temperatures close to their condensation temperatures in the solar nebula.
(2) The textures and mesostasis compositions of Type IA chondrules can be reproduced by melting synthetic AOA. However, the charges lack the complex olivine zonation and the mesostasis silica enrichment trends in chondrules explained by condensation.
(3) The Ca-Al-rich mesostasis in Type IA chondrules might result from melting of either whole CAI, or AOA, or AOA-like dust balls, with liquid–gas interaction. The relict olivine cores in the charges are like relics in chondrules and suggest gradual disruption of an AOA precursor leading to varying amounts of olivine reaction.
(4) In isothermal experiments, relict spinel is present for heating up to 1550 °C but is mostly resorbed by 1600 °C. PO chondrules with no relict spinel could have had higher peak temperatures than 1550 °C and lost evidence of a possible AOA or CAI precursor.
(5) Chondrules with discrete olivine-rich and Ca-Al-rich domains are not common, indicating chondrule melting distinctly higher than condensation temperatures. Fine-grained CAI and chondrules record different events and conditions.
(6) The maximum temperature of 1550 °C for natural spinel-bearing chondrules is a new constraint on chondrule formation conditions. As the spinel-free porphyritic olivine charges resemble Type IA chondrules, there is no requirement that most chondrules formed at near-liquidus temperatures (up to ~1800 °C°).
(7) This 1550 °C spinel disappearance temperature is close to the liquidus temperature of some CAI, consistent with models of chondrule formation by modification by Mg and SiO condensation of RI melt droplets below the liquidus temperatures of the final chondrule compositions.
(8) The oxygen isotopic composition of spinel relict grains in chondrules could indicate their prior environments, particularly because of their slower diffusion rates relative to olivine, which would allow ^{18}O-poor AOA compositions to survive, making spinel a possible key to complex chondrule history.

Declaration of Competing Interest

The authors declare that they have no known competing financial interests or personal relationships that could have appeared to influence the work reported in this paper.

ACKNOWLEDGEMENTS

We thank two anonymous reviewers, D. Shrader, and Y. Marrocchi for detailed comments that led to major improvements in the

paper. RH and SAW acknowledge funding from NASA NNX08AG62G grant awarded to them. The research of JS was supported by the Basic Science Research Program through the National Research Foundation of Korea (NRF) funded by the Ministry of Education (NRF-2019R1I1A1A01063546).

APPENDIX A. SUPPLEMENTARY MATERIAL

Supplementary Fig. S1 Fig. 4 SEM BSE images showing the textural evolution of 1 h synthetic CAI+Fo gel isothermal runs as a function of temperature. Supplementary Fig. S2 SEM BSE images showing examples of 'failed' AOA materials, i.e. ones which were subjected to temperatures and/or durations less than our texturally decided-upon starting run duration and temperature of 200 h–1250 °C. These 'failed' materials do not texturally resemble natural AOA in contrast to the 200 h–1250 °C materials which clearly do (see Fig. 2). Supplementary Table S1 All EPMA data of Fo+AOA and SCO+CAI experimental charges. Supplementary Table S2 Atomic proportions of Fo+AOA and SCO+CAI experimental charges. Supplementary Table S3 EPMA detection limits.

Supplementary data to this article can be found online at https://doi.org/10.1016/j.gca.2021.12.022.

REFERENCES

Aléon J. (2018) Closed system oxygen isotope redistribution in igneous CAIs upon spinel dissolution. *Earth Planet. Sci. Lett.* **482**, 324–333.

Amelin Y., Krot A. N., Hutcheon I. D. and Ulyanov A. A. (2002) Lead isotopic ages of chondrules and calcium–aluminum-rich inclusions. *Science* **297**, 1678–1683.

Beckett J. R. (1986) *The origin of calcium-, aluminum-rich inclusions from carbonaceous chondrites: An experimental study* Ph.D. dissertation. University of Chicago.

Bischoff A. and Keil K. (1983a) Catalog of Al-rich chondrules, inclusions and fragments in ordinary chondrites. In *Special Publication No. 22*. University of New Mexico, Institute of Meteoritics, Albuquerque, pp. 1–33.

Bischoff A. and Keil K. (1983) Ca-Al-rich chondrules and inclusions in ordinary chondrites. *Nature* **303**, 588–592.

Bischoff A. and Keil K. (1984) Al-rich objects in ordinary chondrites: Related origin of carbonaceous and ordinary chondrites and their constituents. *Geochim. Cosmochim. Acta* **48**, 693–709.

Bischoff A., Keil K. and Stoffler D. (1985) Perovskite-hibonite-spinel- bearing inclusions and Al-rich chondrules and fragments in enstatite chondrites. *Chem. Erde* **44**, 97–106.

Bischoff A., Palme H. and Spettel B. (1989) Al-rich chondrules from the Ybbsite H4 chondrite: evidence for formation by collision and splashing. *Earth Planet. Sci. Lett.* **93**, 170–180.

Bollard J., Connelly J. N. and Bizzarro M. (2015) Pb-Pb dating of individual chondrules from the CB_a chondrite Gujba: Assessment of the impact plume formation model. *Meteorit. Planet. Sci.* **50**, 1197–1216.

Borisov A. and Shapkin A. I. (1990) New empirical equation rating Fe^{3+}/Fe^{2+} in magmas to their composition, oxygen fugacity, and temperature. *Geochem. Int.+* **27**, 111–116.

Connelly J. N., Bizzarro M., Krot A. N., Nordlund A., Wielandt D. and Ivanova M. A. (2012) The absolute chronology and thermal processing of solids in the solar protoplanetary disk. *Science* **338**, 651–655. http://refhub.elsevier.com/S0016-7037(16)30622-6/h0130.

Connelly J. N. and Bizzarro M. (2018) The absolute Pb–Pb isotope ages of chondrules. In *Chondrules: Records of Protoplanetary Disk Processes* (eds. S. Russell, H. C. Connolly and A. Krot). Cambridge University Press, pp. 300–323.

Danushevsky L. and Plechov P. (2011) Petrolog 3: Integrated software for modeling crystallization processes. *Geochem. Geophys. Geosy.* **12**.

Connolly, Jr., H. C. and Huss G. R. (2010) Compositional evolution of the protoplanetary disk: Oxygen isotopes of type-II chondrules from CR2 chondrites. *Geochim. Cosmochim. Acta* **74**, 2473–2483.

Ebel D. S. (2006) Condensation of rocky material in astrophysical environments. In *Meteorites and the Early Solar System II* (eds. D. S. Lauretta and H. Y. McSween). The University of Arizona Press, Tucson, pp. 253–277.

Engler A., Varela M. E., Kurat G., Ebel D. and Sylvester P. (2007) The origin of non-porphyritic pyroxene chondrules in UOCs: Liquid solar nebula condensates? *Icarus* **192**, 248–286.

Grossman L. (1972) Condensation in the primitive solar nebula. *Geochim. Cosmochim. Acta* **36**, 597–619.

Grossman J. N. (1988) Formation of chondrules. In *Meteorites and the Early Solar System* (eds. J. F. Kerridge and M. S. Mathews). University of Arizona Press, pp. 680–696.

Hasegawa Y., Wakita S., Matsumoto Y. and Oshino S. (2015) Chondrule formation via impact jetting triggered by planetary accretion. *Astrophys. J.* **816**(1), 8.

Hewins R. H. (1997) Chondrules. *Annu. Rev. Earth Planet. Sci.* **25**, 61–83.

Hewins R. H. and Radomsky P. M. (1990) Temperature conditions for chondrule formation. *Meteoritics* **25**, 309–318.

Hewins R. H., Yu Y., Zanda B. and Bourot-Denise M. (1997) Do nebular fractionations, evaporative losses, or both, influence chondrule compositions? *Antarctic Meteorite Res.* **10**, 275–298.

Hewins R. H. and Fox G. E. (2004) Chondrule textures and precursor grain size: an experimental study. *Geochim. Cosmochim. Acta* **68**, 197–925.

Hewins R. H. and Zanda B. (2012) Chondrules: precursors and interactions with the nebular gas. *Meteorit. Planet. Sci.* **47**, 201–238.

Hewins R. H., Connolly H. C. Jr., Lofgren G. E. and Libourel G. (2005) Experimental constraints on chondrule origins. In *Chondrites and the Protoplanetary* Disk (eds. A. N. Krot, E. R. D. Scott and B. Reipurth), *ASP Conference Series* **341**. Astronomical Society of the Pacific, San Francisco. pp. 286–316.

Hewins R. H., Zanda B. and Bendersky C. (2012) Evaporation and recondensation of sodium in Semarkona Type II chondrules. *Geochim. Cosmochim. Acta* **78**, 1–7.

Hewins R. H., Bourot-Denise M., Zanda B., Leroux H., Barrat J.-A., Humayun M., Göpel C., Greenwood R. C., Franchi I. A., Pont S., Lorand J.-P., Cournède C., Gattacceca J., Rochette P., Kuga M., Marrocchi Y. and Marty B. (2014) The Paris meteorite, the least altered CM chondrite so far. *Geochim. Cosmochim. Acta* **24**, 90–222.

Hewins R., Condie C., Morris M., Richardson M., Oullette N. and Metcalf M. (2018) Thermal history of CB_b chondrules and cooling rate distributions of ejecta plumes. *Astrophys. J. Lett.* **855**, L17 (7pp).

Herzberg C. T. (1979) The solubility of olivine in basaltic liquids: an ionic model. *Geochim. Cosmochim. Acta* **43**, 1241–1251.

Ichikawa O. and Ikeda Y. (1995) Petrology of the Yamato-8449 CR chondrite. *Proceedings of the NIPR Symposium on Antarctica Meteorites* **8**, 63–78.

Itoh S. and Yurimoto H. (2003) Contemporaneous formation of chondrules and refractory inclusions in the early Solar System. *Nature* **423**, 728–731.

Jones R. H. and Scott E. R. D. (1989) Petrology and thermal history of Type IA chondrules in the Semarkona (LL3.0) chondrite. *Proc. Lunar Planet. Sci. Conf.* **19**, 523–536.

Jones R. H., Leshin L. A., Guan Y. B., Sharp Z. D., Durakiewicz T. and Schilk A. J. (2004) Oxygen isotope heterogeneity in chondrules from the Mokoia CV3 carbonaceous chondrite. *Geochim. Cosmochim. Acta* **68**, 3423–3438.

Jones R. H., Grossman J. N. and Rubin A. E. (2005) Chemical, mineralogical and isotopic properties of chondrules: Clues to their origin. In *Chondrites and the Protoplanetary Disk* (eds. A. N. Krot, E. R. D. Scott and B. Reipurth), *ASP Conference Series* **341**. Astronomical Society of the Pacific, San Francisco. pp. 251–285.

Kimura M., Imae N., Komatsu M., Barrat J. A., Greenwood R. C., Yamaguchi A. and Noguchi T. (2020) The most primitive CM chondrites, Asuka 12085, 12169, and 12236, of subtypes 3.0–2.8: Their characteristic features and classification. *Polar Sci.* **26**.

If we quote it for glass composition Komatsu M., Krot A. N., Petaev M. I., Ulyanov A. A., Keil K. and Miyamoto M. (2001) Mineralogy and petrography of amoeboid olivine aggregates from the reduced CV3 chondrites Efremovka, Leoville and Vigarano: Products of nebular condensation, accretion and annealing. *Meteorit. Planet. Sci.* **36**, 629–641.

Komatsu M., Mikouchi T. and Miyamoto M. (2009) High-temperature annealing of amoeboid olivine aggregates: heating experiments on olivine–anorthite mixtures. *Polar Sci.* **3**, 31–55.

Kornacki A. S. and Wood J. A. (1984) Petrography and classification of Ca, Al-rich and olivine-rich inclusions in the Allende CV3 chondrite. *J. Geophys. Res. Solid Earth* **89**, B573–B587.

Krot A. N. and Rubin A. E. (1994) Glass-rich chondrules in ordinary chondrites. *Meteorit. Planet. Sci.* **29**, 697–707.

Krot A. N., Hutcheon I. D. and Keil K. (2002) Plagioclase-rich chondrules in the reduced CV chondrites: Evidence for complex formation history and genetic links between calcium-aluminum-rich inclusions and ferromagnesian chondrules. *Meteorit. Planet. Sci.* **37**, 155–182.

Krot A. N. and Keil K. (2002) Anorthite-rich chondrules in CR and CH carbonaceous chondrites: Genetic link between calcium-aluminum-rich inclusions and ferromagnesian chondrules. *Meteorit. Planet. Sci.* **37**, 91–111.

Krot A. N., Petaev M. I. and Yurimoto H. (2004a) Amoeboid olivine aggregates with low-Ca pyroxenes: A genetic link between refractory inclusions and chondrules? *Geochim. Cosmochim. Acta* **68**, 1923–1941.

Krot A. N., Petaev M. I., Russell S. S., Itoh S., Fagan T. J., Yurimoto H., Chizmadia L., Weisberg M. K., Komatsu M., Ulyanov A. A. and Keil K. (2004b) Amoeboid olivine aggregates and related objects in carbonaceous chondrites: Records of nebular and asteroid processes. *Chem. Erde* **64**, 185–239.

Krot A. N., Amelin Y., Cassen P. and Meibom A. (2005) Young chondrules in CB chondrites from a giant impact in the early Solar System. *Nature* **436**, 989–992.

Krot A. N., McKeegan K. D., Huss G. R., Liffman K., Sahijpal S., Hutcheon I. D. and Keil K. (2006a) Aluminum-magnesium and oxygen isotope study of relict Ca-Al-rich inclusions in chondrules. *Astrophys. J.* **639**, 1227–1237.

Krot A. N., Libourel G. and Chaussidon M. (2006b) Oxygen isotope compositions of chondrules in CR chondrites. *Geochim. Cosmochim. Acta* **70**, 767–779.

Krot A. N. et al. (2009) Origin and chronology of chondritic components: A review. *Geochim. Cosmochim. Acta* **73**, 4963–4997.

Krot A. N. and Nagashima K. (2017) Constraints on mechanisms of chondrule formation from chondrule precursors and chronology of transient heating events in the protoplanetary disk. *Geochem. J.* **51**, 45–68.

Krot A. N., Nagashima K., van Kooten E. M. and Bizzarro M. (2017) Calcium–aluminum-rich inclusions recycled during formation of porphyritic chondrules from CH carbonaceous chondrites. *Geochim. Cosmochim. Acta* **201**, 185–223.

Kruijer T. S., Kleine T. and Borg L. E. (2020) The great isotopic dichotomy of the early Solar System. *Nat. Astron.* **4**, 32–40.

Libourel G., Krot A. N. and Tissandier L. (2006) The role of gas-melt interaction during chondrule formation. *Earth Planet. Sci. Lett.* **251**, 232–240.

Libourel G. and Krot A. N. (2007) Evidence for the presence of planetesimal material among the precursors of magnesian chondrules of nebular origin. *Earth Planet. Sci. Lett.* **254**, 1–8.

Libourel G. and Portail M. (2018) Chondrules as direct thermochemical sensors of solar protoplanetary disk gas. *Sci. Adv.* **4**, eaar3321.

Lin Y., Guan Y., Leshin L. A., Ouyang Z. and Wang D. (2005) Short-live chlorine-36 in a Ca- and Al-rich inclusion from the Ningqiang carbonaceous chondrite. *Proc. Natl. Acad. Sci.* **102**, 1306–1311.

Ma, C., Beckett, J. R., Connolly, H. C., Rossman, G. R. 2008. Aluminous spinels in ferromagnesian chondrules from Allende. In Lunar and Planetary Science Conference (No. 1391, p. 2030).

MacPherson, G, J., 2003. Calcium-aluminum-rich inclusions in chondritic meteorites, In Meteorites, Comet And Planets (ed. A. M. Davis) Vol. 1 Treatise On Geochemistry (eds. H. D. Holland and K. K. Turekian), pp. 201–246. Elsevier-Pergamon, Oxford.

Macpherson G. J. and Grossman L. (1984) "Fluffy" Type A Ca-, Al-rich inclusions in the Allende meteorite. *Geochim. Cosmochim. Acta* **48**, 29–46.

MacPherson G. J. and Huss G. R. (2005) Petrogenesis of Al-rich chondrules: evidence from bulk compositions and phase equilibria. *Geochim. Cosmochim. Acta* **69**, 3099–3127.

MacPherson G. J., Simon S. B., Davis A. M., Grossman L. and Krot A. N. (2005) Calcium–aluminum-rich inclusions: major unanswered questions. In *Chondrites and the Protoplanetary Disk* (eds. A. N. Krot, E. R. D. Scott and B. Reipurth), *ASP Conference Series*, **341**. Astronomical Society of the Pacific, San Francisco. pp. 225–250.

Marrocchi Y., Villeneuve J., Batanova V., Piani L. and Jacquet E. (2018) Oxygen isotopic diversity of chondrule precursors and the nebular origin of chondrules. *Earth Planet. Sci. Lett.* **496**, 132–141.

Marrocchi Y., Euverte R., Villeneuve J., Batanova V., Welsch B., Ferrière L. and Jacquet E. (2019a) Formation of CV chondrules by recycling of amoeboid olivine aggregate-like precursors. *Geochim. Cosmochim. Acta* **247**, 121–141.

Marrocchi Y., Villeneuve J., Jacquet E., Piralla M. and Chaussidon M. (2019b) Rapid condensation of the first Solar System solids. *Proc. Natl. Acad. Sci.* **116**(47), 23461–23466.

Maruyama S. and Yurimoto H. (2003) Relationship among O, Mg isotopes and the petrography of two spinel-bearing compound chondrules. *Geochim. Cosmochim. Acta* **67**, 3943–3957.

Mason B. and Martin P. M. (1977) Geochemical differences among components of the Allende meteorite. *Smithsonian Contrib. Earth Sci.* **19**, 84–95.

McSween, Jr., H. Y. (1977a) Chemical and petrographic constraints on the origin of chondrules and inclusions in carbonaceous chondrites. *Geochim. Cosmochim. Acta* **41**, 601–619.

McSween, Jr., H. Y. (1977b) *Chemical Analyses of Chondrules and Inclusions in Chondrite Meteorites*. Harvard/Smithsonian Center for Astrophysics Report, Cambridge.

Milke R. and Metz P. (2002) Experimental investigation of the kinetics of the reaction wollastonite + calcite + anorthite = grossular + CO_2. *Am. J. Sci.* **302**, 312–345.

Misawa K. and Nakamura N. (1988) Highly fractionated rare-earth elements in ferromagnesian chondrules from the Felix (CO3) meteorite. *Nature* **334**, 47–50.

Misawa K. and Fujita T. (1994) A relict refractory inclusion in a ferromagnesian chondrule from the Allende meteorite. *Nature* **368**, 723–726.

Misawa K. and Nakamura N. (1996) Origin of refractory precursor components of chondrules from carbonaceous chondrites. In *Chondrules and the Protoplanetary Disk* (eds. R. H. Hewins, R. H. Jones and E. R. D. Scott). Cambridge University Press, Cambridge, pp. 99–105.

Nagahara H. and Kushiro I. (1982) Calcium-aluminium-rich chondrules in the unequilibrated ordinary chondrites. *Meteoritics* **17**, 55–63.

Nagahara H., Kita N. T., Ozawa K. and Morishita Y. (2008) Condensation of major elements during chondrule formation and its implication to the origin of chondrules. *Geochim. Cosmochim. Acta* **72**(5), 1442–1465.

Nagahara H., Ozawa K., Tomomura S., 2005. Kinetic condensation of silicate melt and its role in the chemical diversity of chondrules. In Chondrites and the Protoplanetary Disc, 341 (eds. A. N. Krot, E. R. D. Scott and B. Reipurth). APS Conf. Ser, pp. 456–468.

Nazfiger R. H., Ulmer G. C. and Woerman E. (1971) Gaseous buffering for control of oxygen fugacity at one atmosphere. In *Research techniques for high pressure and high temperature* (ed. G. C. Ulmer), pp. 9–41.

Piralla M., Villeneuve J., Batanova V., Jacquet E. and Marrocchi Y. (2021) Conditions of chondrule formation in ordinary chondrites. *Geochim. Cosmochim. Acta* **313**, 295–312.

Rudraswami N. G., Ushikubo T., Nakashima D. and Kita N. T. (2011) Oxygen isotope systematics of chondrules in Allende CV3 chondrite: High precision ion microprobe studies. *Geochim. Cosmochim. Acta* **75**, 7596–7611.

Russell S. S., MacPherson G. J., Leshin L. A. and McKeegan K. D. (2000) ^{16}O enrichments in aluminum-rich chondrules from ordinary chondrites. *Earth Planet. Sci. Lett.* **184**, 57–74.

Ryerson F. J. and McKeegan K. D. (1994) Determination of oxygen self-diffusion in åkermanite, anorthite, diopside, and spinel: Implications for oxygen isotopic anomalies and the thermal histories of Ca-Al-rich inclusions. *Geochim. Cosmochim. Acta* **58**, 3713–3734.

Schneider J. M., Burkhardt C., Marrocchi Y., Brennecka G. A. and Kleine T. (2020) Early evolution of the solar accretion disk inferred from Cr-Ti-O isotopes in individual chondrules. *Earth Planet. Sci. Lett.* **551** 116585.

Schrader D. L., Connolly, Jr., H. C., Lauretta D. S., Nagashima K., Huss G. R., Davidson J. and Domanik K. J. (2013) The formation and alteration of the Renazzo-like carbonaceous chondrites II: Linking O-isotope composition and oxidation state of chondrule olivine. *Geochim. Cosmochim. Acta* **101**, 302–327.

Schrader D. L., Nagashima K., Krot A. N., Ogliore R. C. and Hellebrand E. (2014) Variations in the O-isotope composition of gas during the formation of chondrules from the CR chondrites. *Geochim. Cosmochim. Acta* **132**, 50–74.

Schrader D. L., Nagashima K., Waitukaitis S. R., Davidson J., McCoy T. J., Connolly, Jr, H. C. and Lauretta D. S. (2018) The retention of dust in protoplanetary disks: Evidence from agglomeratic olivine chondrules from the outer Solar System. *Geochim. Cosmochim. Acta* **223**, 405–421.

Schrader D. L., Nagashima K., Davidson J., McCoy T. J., Ogliore R. C. and Fu R. R. (2020) Outward migration of chondrule fragments in the early Solar System: O-isotopic evidence for rocky material crossing the Jupiter Gap? *Geochim. Cosmochim. Acta* **282**, 133–155.

Scott E. R. D. and Krot A. N. (2003) *Chondrites and their components*. Elsevier, Oxford, pp. 143–200.

Sheng Y. J., Hutcheon I. D. and Wasserburg G. J. (1991) Origin of plagioclase-olivine inclusions in carbonaceous chondrites. *Geochim. Cosmochim. Acta* **55**, 581–599.

Stolper E. (1982) Crystallization sequences of Ca-Al-rich inclusions from Allende: an experimental study. *Geochim. Cosmochim. Acta* **46**, 2159–2180.

Taylor G. K., Scott E. R. D. and Keil K. (1983) Cosmic setting for chondrule formation. In *Chondrules and Their Origins* (ed. E. A. King). Lunar and Planetary Institute, Houston, pp. 262–278.

Tenner T. J., Ushikubo T., Kurahashi E., Kita N. T. and Nagahara H. (2013) Oxygen isotope systematics of chondrule phenocrysts from the CO3.0 chondrite Yamato 81020: Evidence for two distinct oxygen isotope reservoirs. *Geochim. Cosmochim. Acta* **102**, 226–245.

Tenner T. J., Nakashima D., Ushikubo T., Kita N. T. and Weisberg M. K. (2015) Oxygen isotope ratios of FeO-poor chondrules in CR3 chondrites: Influence of dust enrichment and H_2O during chondrule formation. *Geochim. Cosmochim. Acta* **148**, 228–250.

Tenner T. J., Kimura M. and Kita N. T. (2017) Oxygen isotope characteristics of chondrules from the Yamato-82094 ungrouped carbonaceous chondrite: Further evidence for common O-isotope environments sampled among carbonaceous chondrites. *Meteorit. Planet. Sci.* **52**, 268–294.

Tenner T. J., Ushikubo T., Nakashima D., Schrader D. L., Weisberg M. K., Kimura M. and Kita N. (2018) Oxygen isotope characteristics of chondrules from recent studies by secondary ion mass spectrometry. In *Chondrules: Records of the Protoplanetary Disk Processes* (eds. S. S. Russell, H. C. Connolly and A. N. Krot). Cambridge Univ. Press, Cambridge, pp. 196–246.

Tissandier L., Libourel G. and Robert F. (2002) Gas-melt interactions and their bearing on chondrule formation. *Meteorit. Planet. Sci.* **37**, 1377–1389.

Toppani A., Libourel G., Robert F. and Ghambaja J. (2006) Laboratory condensation of refractory dust in protosolar and circumstellar conditions. *Geochim. Cosmochim. Acta* **70**, 5035–5060.

Tronche E. J., Hewins R. H. and MacPherson G. J. (2007) Formation conditions of aluminum-rich chondrules. *Geochim. Cosmochim. Acta* **70**, 336–338.

Varela M. E., Kurat G. and Zinner E. (2006) The primary liquid condensation model and the origin of barred olivine chondrules. *Icarus* **184**, 344–364.

Villeneuve J., Libourel G. and Soulié C. (2015) Relationships between type I and type II chondrules: Implications on chondrule formation processes. *Geochim. Cosmochim. Acta* **160**, 277–305.

Wark D. A. (1987) Plagioclase-rich inclusions in carbonaceous chondrite meteorites: Liquid condensates? *Geochim. Cosmochim. Acta* **51**, 221–242.

Warren P. H. (2011) Stable-isotopic anomalies and the accretionary assemblage of the Earth and Mars: A subordinate role

for carbonaceous chondrites. *Earth Planet. Sci. Lett.* **311**(1–2), 93–100.

Weisberg M. K., Connolly, Jr, H. C. and Ebel D. S. (2004) Petrology and origin of amoeboid olivine aggregates in CR chondrites. *Meteorit. Planet. Sci.* **39**, 1741–1753.

Whattam S. A. and Hewins R. H. (2009) An origin for PO chondrules from thermally annealed granoblastic olivine aggregates. *Geochim. Cosmochim. Acta* **73**, 5460–5482.

Whattam S. A., Hewins R. H., Cohen B. A., Seaton N. C. and Prior D. J. (2008) Granoblastic olivine aggregates in magnesian chondrules: planetesimal fragments or thermally annealed solar nebula condensates? *Earth Planet. Sci. Lett.* **269**, 200–211.

Williams C. D., Sanborn M. E., Defouilloy C., Yin Q. Z., Kita N. T., Ebel D. S. and Yamashita K. (2020) Chondrules reveal large-scale outward transport of inner Solar System materials in the protoplanetary disk. *Proc. Natl. Acad. Sci.* **117**, 23426–23435.

Wood J. A. and Hashimoto A. (1993) Mineral equilibrium in fractionated nebular systems. *Geochim. Cosmochim. Acta* **57**, 2377–2388.

Zhang M., Lin Y., Tang G., Liu Y. and Leya I. (2020) Origin of Al-rich chondrules in CV chondrites: Incorporation of diverse refractory components into the ferromagnesian chondrule-forming region. *Geochim. Cosmochim. Acta* **272**, 198–217.

Associate editor: Yves Marrocchi